Research Square

Preprints are preliminary reports that have not undergone peer review.
They should not be considered conclusive, used to inform clinical practice,
or referenced by the media as validated information.

Chondrule Fragments in Particles from the Carbonaceous Asteroid (101955) Bennu

Kathie Thomas-Keprta

kathie.thomas-keprta-1@nasa.gov

Johnson Space Center/Barrios Technology (JETS)

Loan Le

Amentum https://orcid.org/0000-0002-6760-2431

Simon Clemett

NASA Johnson Space Center

Laura Seifert

NASA Johnson Space Center https://orcid.org/0000-0001-6044-4226

Lindsay Keller

NASA Johnson Space Center https://orcid.org/0000-0003-1560-2939

Ann Nguyen

NASA Johnson Space Center https://orcid.org/0000-0002-0442-1991

Roger Harrington

Amentum, NASA JSC

Romy Hanna

The University of Texas at Austin https://orcid.org/0000-0002-2102-8040

Zia Rahman

Amentum, NASA Johnson Space Center https://orcid.org/0000-0002-4923-767X

Timmons Erickson

Jacobs - JETS, NASA Johnson Space Center https://orcid.org/0000-0003-4520-7294

Leonard Suess

Amentum, NASA JSC

Jennifer Gorce

Amentum, NASA JSC

Tim McCoy

Smithsonian Institution

Thomas Zega

University of Arizona https://orcid.org/0000-0002-9549-022X

Sara Russell

Natural History Museum

Harold Connolly Jr

Rowan University, School of Earth and Environment https://orcid.org/0000-0002-1803-5098

Dante Lauretta

University of Arizona https://orcid.org/0000-0002-2597-5950

Article

Keywords:

Posted Date: March 20th, 2026

DOI: https://doi.org/10.21203/rs.3.rs-8896456/v1

License: This work is licensed under a Creative Commons Attribution 4.0 International License.
Read Full License

Additional Declarations: There is **NO** Competing Interest.

Table of Contents

Table of Contents i
Chondrule Fragments in Particles from the Carbonaceous Asteroid (101955) Bennu 1
Abstract 1
Introduction 2
Results 2
Composition and Mineralogy of Chondrule Fragment in OREX-803437-100 3
Composition and Mineralogy of Chondrule Fragments in OREX-803079-241 5
Oxygen Isotopic Analyses of Olivine in OREX-803437-100 and OREX-803079-241 Chondrule Fragments 7
Discussion 8
Differences from chondrules in carbonaceous chondrites & implications for parent-body history 9
References 12
Acknowledgments 16
Author Contributions 17
Data Availability 17
Methods 18
Sample Preparation and Analysis Sequence 18
Analytical Techniques 19
Figures 23
Extended Data Figures 32
Extended Data Tables 41

Chondrule Fragments in Particles from the Carbonaceous Asteroid (101955) Bennu

Kathie Thomas-Keprta[1], Loan Le[2], Simon Clemett[3], Laura B. Seifert[4], Lindsay P. Keller[4], Ann N. Nguyen[4], Roger Harrington[2], Romy Hanna[5], Zia Rahman[2], Timmons Erickson[2], Leonard Suess[6], Jennifer Gorce[2], Tim J. McCoy[7], Tom J. Zega[8], Sara S. Russell[9], Harold C. Connolly Jr.[8,10,11], and Dante S. Lauretta[8]

[1]Barrios/Amentum, NASA Johnson Space Center (JSC), Houston, TX, USA (kathie.thomas-keprta-1@nasa.gov)
[2]Amentum, NASA JSC, Houston, TX, USA
[3]Asterion/Amentum, NASA JSC, Houston, TX, USA
[4]Astromaterials Research and Exploration Science Division (ARES), NASA JSC, Houston, TX, USA
[5]Department of Earth and Planetary Sciences, University of Texas, Austin, TX, USA
[6]Jacobs, NASA JSC, Houston, TX, USA
[7]National Museum of Natural History, Smithsonian, Washington, D.C., USA
[8]Lunar and Planetary Laboratory, University Arizona, Tucson, AZ, USA
[9]Natural History Museum, London, UK
[10]Department of Geology, School of Earth and Environment, Rowan University, Glassboro, NJ, USA
[11]Department of Earth & Planetary Sciences, American Museum of Natural History, NY, USA

Abstract

Chondrules are one of the first solid materials that formed during the birth of the Solar System and their study in primitive meteorites has been consequential in understanding the conditions and processes in which the building blocks of the planets, and chondrites, formed. However, chondrules are absent in the most aqueously altered meteorites, the Ivuna-like (CI) carbonaceous chondrites. Samples from the asteroid (101955) Bennu, returned by NASA's OSIRIS-REx mission, resemble CI chondrites in composition and mineralogy. Here we show that some Bennu particles nevertheless contain numerous chondrule fragments. Although these fragments share many traits of porphyritic and non-porphyritic (barred olivine and radial pyroxene) chondrules observed in non-CI carbonaceous chondrites, they lack any discernible mesostasis or typical secondary phyllosilicate replacement phases. We conclude that aqueous alteration in Bennu's parent body removed any mesostasis present within the chondrule fragments but did not

completely erase or replace their mineralogy. Our findings distinguish the Bennu samples from the CI chondrites and help constrain the reservoir from which Bennu's parent body formed and the geologic processes that occurred within it.

Introduction

Bennu is a near-Earth, rubble-pile asteroid consisting of reaccumulated fragments from a primitive carbonaceous progenitor (or parent body) that was destroyed in a collision (*e.g.,*[1,2] and references therein). The OSIRIS-REx spacecraft delivered regolith collected from Bennu's surface to Earth in 2023[1]. Analyses of these samples revealed a mineralogy dominated by phyllosilicates and bulk element abundances that are comparable to those of the most aqueously altered carbonaceous chondrites [3–5]. Given the paucity of unaltered (anhydrous) mafic silicates (no more than a few volume percent), there was little initial expectation that chondrules or their pseudomorphs could have survived the implied aqueous alteration on Bennu's progenitor asteroid, a scenario having been previously invoked to explain the absence of chondrules in the extensively aqueously altered CI chondrites[6].

However, some anhydrous silicates in the Bennu samples exhibit chondrule-like oxygen isotope compositions[7,8] and Mn/Fe ratios[4]. We searched ~ 100 Bennu particles for chondrules (whole, fragments, or pseudomorphs), using their distinctive igneous (*i.e.*, melt-grown) textures, mineralogy, and isotopic compositions as criteria to recognize them[9–14] (see Methods).

Results

We did not observe whole chondrules or pseudomorphs, but we found seven Bennu particles that collectively contain 91 chondrule fragments (Extended Data Table 1). Five of these particles belong to Bennu's hummocky lithology and two to its angular lithology[5,15]. The observed chondrule fragments were subjected to a series of coordinated analyses to document their textures and compositions including optical microscopy, field emission scanning electron microscopy (FESEM), scanning transmission electron microscopy (STEM), energy-dispersive X-ray spectroscopy (EDX), selected-area electron diffraction (SAED), electron microprobe, electron

backscatter diffraction (EBSD), X-ray computed tomography (XCT), and nanoscale secondary ion mass spectrometry (NanoSIMS). The analysis sequence for each particle is described in the Methods.

The emphasis of this study is on four of these particles that comprise the majority and represent the different types of chondrule fragments we observed (*e.g.,*[10,14,16–20]) (Extended Data Table 1): OREX-803437-100, OREX-803079-241, OREX-803417-103, and OREX-803429-100. Particle OREX-803437-100 contains a type I (FeO-poor) porphyritic olivine pyroxene (POP) fragment. Particles OREX-803079-241 and OREX-803417-103 collectively contain 84 type I barred olivine pyroxene (BOP) fragments (some of which may also be transitional with radial textures[21]) and OREX-803079-241 also contains a single type I radial pyroxene olivine (RPO) fragment. Particle OREX-803429-100 contains a type II (FeO-bearing) BOP chondrule fragment.

Composition and Mineralogy of Chondrule Fragment in OREX-803437-100

Bennu particle OREX-803437-100 is triangular with rounded vertices (Fig. 1a). The surface of the particle shows fine-grained phyllosilicate matrix containing nanophase Fe-sulfides and magnetite. After polishing, the particle exhibits two distinct regions (Fig. 1b): the upper region is composed of fine-grained phyllosilicate matrix, whereas the lower region comprises a chondrule fragment that represents ~ ½ of the particle (~ 450 × 180 μm^2). The fragment is composed of fractured, irregular grains of Mg-rich olivine and low Ca-pyroxene with lesser abundances of Ca-bearing pyroxene, carbonates (dolomite, calcite), and Fe-Ni metal (likely kamacite) present as micron-sized spheroids (Fig. 1b). Within the fragment, we did not observe mesostasis — the last solidified liquid within chondrules, which is glassy (feldspar normative) or composed of glass plus fine crystallites that bind melt-grown crystals together — or abundant secondary replacement minerals such as phyllosilicates.

Major element compositions of olivines (avg. Mg #99) and low-Ca pyroxenes (avg. Mg #99), determined from FESEM-EDX point analyses (Extended Data Table 2), fall within the range for silicates in chondrules found in Mighei-like (CM2)[22], Renazzo-like (CR2)[23], and Vigarano-like (CV3)[23] chondrules (the numbers attached to the abbreviations indicate petrologic grade in the scheme of Van Schmus and Wood[24]) (Fig. 2a). Minor element abundances for fragment olivines and pyroxenes are within the range of type I chondrules in primitive carbonaceous chondrites —

the average olivine composition of the fragment is comparable in Cr_2O_3 and CaO abundances to that of type I chondrules in primitive carbonaceous chondrites (petrologic grade $\leq$ 3.0) (Fig. 2b). Plots of minor oxides CaO, MnO, and Cr_2O_3 versus FeO of fragment olivine (Fig. 2c) fall within ranges for olivines in type I carbonaceous chondrite chondrules[25–28]. Rounded Fe-Ni metal inclusions are present in some olivine grains (Fig. 1b) as often observed in porphyritic chondrules[29].

Numerous lens-shaped pits and serrated sawtooth features (Fig. 1a), potentially from aqueous etching, occur in the low-Ca pyroxene particles that are also overlain with rare serpentine-type phyllosilicates with compositions ranging between Mg-rich (*e.g.*, antigorite; $Mg_3Si_2O_5(OH)_4$) and Fe-rich (greenalite; $Fe_3Si_2O_5(OH)_4$) endmembers. Secondary Fe-rich and Mg-rich phases (Fig. 1b; Extended Data Table 2; Extended Data Fig. 1) border anhydrous Mg-rich silicate grains in the chondrule fragment.

TEM characterization of a focused ion beam (FIB) section (OREX-800070-104) extracted from a region in OREX-803437-100 containing both Fe- and Mg-rich secondary phases (Extended Data Fig. 1) shows the former having a lath-like texture and the latter composed of interlaced fibers (Extended Data Fig. 2). Based on lattice fringe measurements from high-resolution TEM imaging, the Fe-rich region is composed of two discrete Fe(III) oxyhydroxide phases, lepidocrocite (γ-FEOOH) and akaganeite (β-FeOOH) (Extended Data Fig. 2d), and the sinuous fibers comprising the Mg-rich region (Extended Data Fig. 2h) are primarily amorphous or poorly crystalline, with some regions exhibiting lattice spacings of ~ 0.62 nm. The Mg-rich regions may be mixtures of various low-temperature phases (*e.g.*, modified brucite-like phase(s) and ferrihydrite ($Fe_2O_3{\cdot}0.5(H_2O)$)) that degrade under electron beam exposure (Extended Data Fig. 1d, inset). Dispersed among the Fe-rich fibers are discrete Si-, Al-, S-rich regions (< 200 nm in size), *e.g.*, fine-grained phyllosilicate matrix with embedded sulfides and magnetite, and nanophase chromite grains (Extended Data Fig. 2b, c). Si-rich hotspots, possibly fine-grained matrix, are also distributed among the Mg-rich fibers (Extended Data Fig. 2f, g).

The bulk Mg:Si ratio (wt%) for the chondrule fragment is 1.28, for the bulk matrix is 0.92, and for the bulk particle is 1.21 (based on FESEM-EDX analysis of the entire particle; Extended Data Table 2). For comparison, the Mg:Si ratio of bulk chondrules is ~1.10 in the Murchison CM2

chondrite[30] and 1.03 ± 0.2 in the Renazzo CR2 chondrite[31], with the Mg:Si ratios of bulk particles being 0.90–0.91 for CI[32], CM[31,32], and CR[32] chondrites. The chondrule fragment in this Bennu particle is depleted in Si, likely due to the absence of siliceous mesostasis or replacement phyllosilicates.

Composition and Mineralogy of Chondrule Fragments in OREX-803079-241

Particle OREX-803079-241, ~ 1 mm in length, has a pseudo-parallelogram morphology and an irregular surface texture (Fig. 3a). Using optical microscopy, the particle topside and underside were imaged. Common to both are light-colored chondrule fragments that contrast with the darker matrix. Three of these fragments were identified on the particle topside (Fig. 3a), including one larger fragment with a barred texture (~ 150 μm in length; Fig. 3b), a smaller fragment with a similarly barred texture (~ 75 μm in length; Fig. 3a), and a fragment with an acicular/fibrous texture (~ 165 μm in length; Fig. 3c). Additional light-colored regions cascading along an edge of the particle are composed of euhedral calcite crystals ranging from ~ 1 to 3 μm in size. Six light-colored fragments were identified on the underside of the particle, all displaying barred textures identical to those observed on the topside.

The barred fragments on the particle topside are composed primarily of Mg-rich olivine with minor low Ca-pyroxene (Extended Data Table 3) with barred fragments on the underside having identical compositions. Barred fragments are arranged as stacks of semi-parallel plates ~ 1–5 μm in width and separated by void space (Fig. 3b). The plates manifest a perforated texture with rounded edges and pore sizes ranging from ~ 1 to 3 μm (Fig. 3b, inset), indicating that these are fragments of chondrules. Both barred fragments on the topside consist predominantly of forsteritic olivine with Mg# 96–98 and also contain minor low Ca-pyroxene with Mg# 98–100. Distributed among the olivine plates are micron-sized clumps of fine-grained matrix material containing sub-micron Fe-sulfides and framboidal magnetite (Fig. 3b, inset), indicating that some matrix material was displaced, possibly during sample preparation or particle movement in the sample return capsule during Earth reentry. No mesostasis was detected, and there is little to no evidence of replacement minerals associated with the pore spaces in either the barred or acicular fragments. Three of the six barred fragments on the underside contain several clusters, up to ~ 2

μm across, of secondary phyllosilicate minerals. These clusters differ from the surrounding matrix, being devoid of nanophase Fe-bearing minerals.

A FIB section was extracted from near the center of the larger barred fragment on the particle topside (OREX-803079-100; Fig. 3b). The FIB section contains elongated grains of Mg-rich olivine and low-Ca pyroxene, consistent with FESEM observations, together with small crystals of pyrrhotite, pentlandite, and chromite (Extended Data Fig. 3). No mesostasis or replacement phyllosilicates were detected within pore spaces.

The fibrous, acicular fragment is located ~ 25 μm from the larger barred fragment on the particle topside (Fig. 3a, c). Although individual fiber lengths are difficult to constrain, they typically have sub-micron diameters and appear loosely aligned, with some converging toward a single point (Fig. 3c, inset). This fragment exhibits a high degree of porosity between crystals, and many of the acicular crystals contain small, irregular-shaped perforations (Fig. 3c, inset). The average Mg:Si ratio (wt%) ranges from 1.04 to 1.13 (Extended Data Table 3), consistent with a mixture of Mg-bearing olivine and Mg-bearing pyroxene. Interspersed among the acicular crystals are micron-sized clumps of fine-grained phyllosilicate matrix with embedded Fe-sulfides, magnetite, and chromite.

A FIB section was extracted near the center of the acicular fragment (OREX-803079-101; Fig. 3c), and high-resolution TEM-EDX and SAED analyses confirm that the acicular crystals are composed of Mg-rich olivine and low-Ca pyroxene, the latter as fine-scale intergrowths of clino- and ortho-enstatite polymorphs (Extended Data Fig. 4). There is no evidence for either mesostasis or replacement minerals associated with the pore space.

XCT analysis of OREX-803079-241 reveals an additional ~ 35 fragments with barred (some possibly with transitional with radial textures) located within the interior of the particle (Supplementary Data Video 1). One of the largest barred fragments is centrally located and composed of semi-parallel bars, identical in texture to the barred fragments on the outer particle surfaces (Supplementary Data Video 2). To access the centrally located barred fragment, the particle was embedded in epoxy and polished to expose a fresh internal surface that also contained 20 barred fragments ranging from ~ 10–90 μm in size (Fig. 4a, b). After polishing, the center fragment displays a pseudo-rectangular shape composed of irregular shaped grains (Fig.

4a, c; labeled #1) and consists primarily of Mg-rich olivine, with lesser low-Ca pyroxene and rare high-Ca pyroxene (Extended Data Table 4). Mean compositions of fragments #2–20 (Extended Data Table 4) indicate Mg-rich olivine and Mg-rich, low-Ca pyroxene with an average Mg:Si of 1.59. Dark regions surrounding the silicate grains are filled with epoxy, indicating abundant pore space between bars. Although phyllosilicates were not identified, several Mg-rich phases are present within the void space (Fig. 4d; Extended Data Table 4), and their Mg:Si ratio within the range of that of the Mg-rich phases observed in OREX-803437-100 (Extended Data Figs. 1d, f and 2e-h; Extended Data Table 2), although they are highly enriched in Cr (7.0 wt% Cr in OREX-803079-241 vs. 1.4 wt% Cr in OREX-803437-100). Two Ca- and Al-rich hotspots (Fig. 4c, e) are identified within olivine laminae. EBSD inverse pole data (not shown) reveals that the silicate bars in fragment #1 (Fig. 4a, f) share a common crystallographic orientation, elongated along the c-axis [001] and oriented normal to the b-axis [010] of forsterite (Fig. 4g, h).

Major element composition of olivines and pyroxenes in the OREX-803079-241 barred and acicular fragments (Fig. 2a) fall within the range for silicates in the chondrules of CM2[22], CR2[23] and CV3[23] chondrites. The average olivine composition of internal barred fragments (calculated for the polished surface) is comparable in Cr_2O_3 and CaO abundances to that of type I chondrules in primitive carbonaceous chondrites (petrologic grade $\leq$ 3.0) (Fig. 2b). Plots of minor oxides CaO, MnO, and Cr_2O_3 versus FeO for barred olivine grains (Fig. 2c) fall within the compositional ranges for olivines in type I chondrules of carbonaceous chondrites [25–28].

For a detailed description of the composition and mineralogy of chondrule fragments in OREX-803417-103 and OREX-803429-100, see Fig. 5, Extended Data Table 5 and the Supplementary Text.

Oxygen Isotopic Analyses of Olivine in OREX-803437-100 and OREX-803079-241 Chondrule Fragments

Bulk oxygen isotopic ratios ($\delta^{18}O$ and $\delta^{17}O$) of Mg-rich olivine were measured in the chondrule fragments from particles OREX-803437-100 and OREX-803079-241 (Fig. 6). Mg-rich olivines in the chondrule fragment in particle OREX-803079-241 have a bulk $\delta^{18}O$ and $\delta^{17}O$ value of –5.8 $\pm$ 1.8‰ and –7.6 $\pm$ 3.4‰, respectively, plotting slightly above the Primitive Chondrule Minerals (PCM) line[33]. In contrast, the barred olivine in particle OREX-803437-100 yields $\delta^{18}O$ and $\delta^{17}O$ values of

232 0.7 ± 0.7‰ and –1.8 ± 2.6‰, respectively, and fall along the PCM line. For comparison, Fig. 6
233 includes oxygen-isotopic ratios of chondrule olivines in carbonaceous chondrites of petrologic
234 grade ≤ 3.0 (CM[27], CV[29, 30], CR[29], Ornans-like (CO)[31, 32], and Tagish Lake (ungrouped)[28]), as well as
235 in samples from the carbonaceous asteroid (162173) Ryugu[16] and Comet 81P/Wild 2[26]. Four
236 analyses of a bulk Bennu sample yielded weighted averages of $\delta^{17}O$ = 11.2 ± 0.8‰ and $\delta^{18}O$ =
237 20.2 ± 1.8‰[8].

238 ## Discussion

239 Ninety-one features identified in seven Bennu particles exhibit physical, chemical, and
240 isotopic properties that unambiguously classify them as chondrule fragments, albeit with novel
241 traits. These fragments encompass three chondrule classes: [1] porphyritic olivine pyroxene; [2]
242 barred olivine pyroxene; and [3] radial pyroxene olivine. Of these, the majority are type I (low
243 FeO) barred olivine pyroxene chondrule fragments; only a single type II (high FeO) barred olivine
244 pyroxene fragment was identified. Neither mineral zonation nor accretionary rims were observed
245 in any of the fragments, possibly owing to the absence of intact, whole chondrules. A
246 comparative summary of the characteristics of Bennu particles and aqueously altered
247 carbonaceous chondrites is presented in Extended Data Table 6.

248 In the two Bennu particles containing multiple chondrule fragments (OREX-803079-241 and
249 OREX-803417-103), the width and spacing of olivine blades in individual fragments are nearly
250 identical within each particle. This observation suggests that all the fragments within a given
251 particle were derived from same parent chondrule, which was likely fractured during accretion
252 and subsequent incorporation into Bennu's parent body. Similarly, multiple episodes of
253 chondrule fracturing and deformation have been proposed to be recorded in the Murchison
254 meteorite[25].

255 A small but significant fraction of chondrules within carbonaceous chondrites contain relic
256 grains (*e.g.*,[9,34–36]) that did not crystallize *in situ* within the host chondrule and are interpreted as
257 remnants of precursor materials. Among the Bennu chondrules fragments identified here, we
258 note two tentative instances of similar relic materials: In the POP chondrule fragment in OREX-
259 803437-100, Ni-poor Fe-metal inclusions are present within olivine (Fig. 1b), and in one of the

barred olivine chondrule fragments in OREX-803079-241, two micron-sized Al- and Ca-rich hotspots (Fig. 4c, e) are observed.

Differences from chondrules in carbonaceous chondrites & implications for parent-body history

In carbonaceous chondrites, mesostasis is commonly replaced by phyllosilicates during aqueous alteration on the parent body. Although the Bennu chondrule fragments show affinities to those in aqueously altered carbonaceous chondrites (*e.g.,*[7,8,11,12,24]) and to chondrule-like objects in Ryugu samples[16], they are distinct in being devoid of mesostasis (*i.e.*, typically feldspathic-like[7]) and of abundant secondary replacement minerals such as phyllosilicates. This distinction is significant because there are no previous reports in the literature of porous chondrules lacking infilling mesostasis and/or replacement phyllosilicates, with the sole possible exception being a single chondrule-like cryptocrystalline forsterite reported in the Murchison meteorite[37].

Comparable, though less extensive, mesostasis-depleted textures have been reported[38] in petrologic grade 3 ordinary chondrites, where partial bleaching and void formation within chondrule interiors were attributed to localized aqueous alteration. The Bennu chondrule fragments may represent a more advanced expression of this process, in which mesostasis removal was complete and no replacement phases subsequently developed. Alternatively, experimental studies have shown that internal pore networks can form during chondrule crystallization through liquid contraction[39]. The geometry of the pores in Bennu's barred and radial fragments is consistent with such a primary origin. However, the complete absence of mesostasis, and the presence of aqueous corrosion textures and secondary Fe- and Mg-bearing phases, indicate that these primary cavities were subsequently modified by dissolution of any mesostasis. The voids observed today thus likely represent relic igneous architecture reshaped by parent-body aqueous alteration.

Our observations imply three possible scenarios: [1] mesostasis was never present, or only present in very minor amounts, in the Bennu chondrule fragments; [2] mass transport during aqueous dissolution of mesostasis prevented in-place phyllosilicate reprecipitation; or [3] a combination of [1] and [2]. The first scenario is not impossible, as shown by experimental work[39] where supercooled liquid rapidly crystallizes to form barred to radial (even transitional) textures

with pore spaces between the individual crystals. There has been no systematic investigation of radial or barred-to-radial transitional textures in chondrules; thus, the potential abundances of nonporphyritic textures with pore spaces is not known and it should not be assumed that they all must have had mesostasis.

The second scenario assumes that the chondrule fragments in our investigation did have mesostasis, perhaps a small amount, prior to fragmentation and subsequent accretion into the surrounding matrix. In this scenario, we infer that Bennu's progenitor body experienced an aqueous alteration history unlike that recorded in known carbonaceous chondrites, one that prevented in-place phyllosilicate replacement of mesostasis. Independent evidence indicates that Bennu particles underwent multiple episodes of low-temperature aqueous alteration by alkaline, saline fluids[3,4]. Furthermore, all the Bennu particles in which we observed chondrule fragments also contained extensive networks of open veins and channels and this is illustrated by particle OREX-803437-100, which was immersed in epoxy resin (without applied pressure) prior to polishing. The resin infiltrated the pore space within a large barred chondrule fragment located at the center of the particle (see Fig. 4). The infiltration of these voids by high-viscosity epoxy suggests that lower-viscosity fluid, such as water, would have readily permeated the chondrule fragment and dissolved the mesostasis. Based on the composition of secondary phases in particles OREX-803437-100 (Extended Data Table 2), OREX-8030279-241 (Extended Data Table 4), and OREX- 803417-103 (Extended Data Table 5), the altering fluid was likely depleted in Si and enriched in Mg, Al, and Fe (along with alkali metals Na, K), thereby limiting phyllosilicate formation.

Finally, notwithstanding the documented resemblances between Bennu samples and CI chondrites (*e.g.,* [4,8,15]), the latter do not contain chondrules or fragments thereof. Thus, either the reservoir from which Bennu's parent body accreted differed in the abundance of chondrules and/or chondrule fragments from that of CI chondrites, and/or the degree of aqueous alteration experienced by Bennu particles that host chondrule fragments was less than that experienced by all CI chondrites.

While all Bennu particles analyzed to date generally show evidence of extensive interaction with aqueous fluids, the analyses of chondrule fragments presented here suggest a complex and

318 nuanced history of dissolution and reprecipitation within the parent body (see Supplementary
319 Text, 'On the Nature of the Fluid After Mesostasis Dissolution'). The oxygen isotopic diversity
320 among the Bennu fragments further demonstrates that materials from isotopically distinct
321 nebular reservoirs were incorporated into a single parent body (see Supplementary Text,
322 'Isotopic Heterogeneity in Bennu Chondrule Fragments'). Together, these findings reveal an
323 alteration environment and material assemblage not represented in existing meteorite
324 collections, underscoring Bennu's role as a repository of previously unsampled carbonaceous
325 lithologies.

References

1. Lauretta, D. S. *et al.* The unexpected surface of asteroid (101955) Bennu. *Nature* **568**, (2019).
2. Botte, W., Ghent, R., Mazrouei, S., Robbins, S. & Vokrouhlicky, D. Asteroid Impacts, Crater Scaling Laws, and a Proposed Younger Age for Venus's Surface. in *American Astronomical Society* id 201.07 (2015).
3. McCoy, T. J. *et al.* An evaporite sequence from ancient brine recorded in Bennu samples. *Nature* **637**, 1072–1077 (2025).
4. Zega, T. J. *et al.* Mineralogical evidence for hydrothermal alteration of Bennu samples. *Nature Geoscience* **18**, 832–839 (2025).
5. Connolly, H. C. *et al.* An overview of the petrography and petrology of particles from aggregate sample from asteroid Bennu. *Meteoritics and Planetary Science* **60**, 979–996 (2025).
6. Kimura, M., Ito, M., Monoi & Yamaguchi, A. The primary abundance of chondrules in CI chondrites. *Geochimica et Cosmochimica Acta* **378**, 36–44 (2024).
7. Russell, S. S. *et al.* Anhydrous minerals in asteroid Bennu: Evidence for well-preserved primordial components. *Meteoritics and Planetary Science* **In review**, (2026).
8. Barnes, J. J. *et al.* The variety and origin of materials accreted by Bennu's parent asteroid. *Nature Astronomy* **9**, 1785–1802 (2025).
9. Jones, R. H., Grossman, J. N. & Rubin, A. Chemical, mineralogical and isotopic properties of chondrules: Clues to their origin. in *Chondrites and the Protoplanetary Disk* vol. 341 (2005).
10. Hewins, R. Chondrules. *Annual review of Earth and Planetary Sciences* **25**, (2024).
11. Hewins, R. Chondrules and the protoplanetary disk: an overview. in *Chondrules and the Protoplanetary Disk* 3–9 (Cambridge University Press, Cambridge, 2011).
12. Jones, R. H., Villeneuve, J. & Libourel, G. Thermal histories of chondrules: Petrologic observations and experimental constraints. in *Chondrules: Records of Protoplanetary Disk Processes* 57–90 (Cambridge University Press, 2018).
13. Zolensky, M. E. *et al.* Chapter 2 - Physical, Chemical, and Petrological Characteristics of Chondritic Materials and Their Relationships to Small Solar System Bodies. in *Primitive*

Meteorites and Asteroids (ed. Abreu, N.) 59–204 (Elsevier, 2018). doi:10.1016/B978-0-12-813325-5.00002-1.

14. Connolly Jr., H. C. & Jones, R. H. Chondrules: The canonical and noncanonical views. *Journal of Geophysical Research: Planets* **121**, 1885–1899 (2016).
15. Lauretta, D. S. *et al.* Asteroid (101955) Bennu in the laboratory: Properties of the sample collected by OSIRIS-REx. *Meteoritics & Planetary Science* **59**, 2453–2486 (2024).
16. Friend, P., Hezel, D., Barrat, J. A., Zipfel, J. & Palme, H. The chemical composition of matrix, chondrules and bulk of the CM chondrite Jbilet Winselwan. in Abst # 1893 (Houston, Texas, 2016).
17. Grossman, J. N., Rubin, A. E., Nagahara, H. & King, E. A. Properties of Chondrules. in *Meteorites and the Early Solar System* 619–659 (University of Arizona Press, Tucson, 1988).
18. Hutchison, R., Bridges, J. C. & Gilmour, J. D. Chondrules: Chemical, Petrographic and Chronologic Clues to Their Origin by Impact. in *Chondrites and the Protoplanetary Disk* vol. 341 933–950 (San Francisco, CA, 2005).
19. Zanda, B. Chondrules. *Earth and Planetary Science Letters* **224**, 1–17 (2004).
20. Marrocchi, Y. *et al.* Chondrule properties and formation conditions. *Space Science Reviews* **220**, 69–168 (2024).
21. Connolly Jr., H. C. & Hewins, R. H. Chondrules as products of dust collisions with totally molten droplets within a dust-rich nebular environment: An experimental investigation. *Geochimica et Cosmochimica Acta* **59**, 3231–3246 (1995).
22. Rubin, A. E. & Wasson, J. T. Chondrules in the Murray CM2 meteorite and compositional differences between CM-CO and ordinary chondrite chondrules. *Geochimica et Cosmochimica Acta* **50**, 307–315 (1986).
23. Olsen, M. B., Wielandt, D., Schiller, M., Van Kooten, E. M. M. E. & Bizzarro, M. Magnesium and 54Cr isotope compositions of carbonaceous chondrite chondrules – Insights into early disk processes. *Geochimica et Cosmochimica Acta* **191**, 118–138 (2016).
24. Van Schmus, W. R. & Wood, J. A. A chemical-petrologic classification for the chondritic meteorites. *Geochimica et Cosmochimica Acta* **31**, 747–765 (1967).

25. Nakashima, D. *et al.* Chondrule-like objects and Ca-Al-rich inclusions in Ryugu may potentially be the oldest Solar System materials. *Nature Communications* **14**, 532 (2023).
26. Schrader, D. L. *et al.* The formation and alteration of the Renazzo-like carbonaceous chondrites III: Toward understanding the genesis of ferromagnesian chondrules. *Meteoritics and Planetary Science* **50**, 15–50 (2015).
27. Schrader, D. L. & Davidson, J. CM and CO chondrites: A common parent body or asteroidal neighbors? Insights from chondrule silicates. *Geochimica et Cosmochimica Acta* **214**, 157–171 (2017).
28. Jacquet, E., Piralla, M., Kersaho, P. & Marrocchi, Y. Origin of isolated olivine grains in carbonaceous chondrites. *Meteoritics and Planetary Science* **56**, 13–33 (2021).
29. Libourel, G. & Portail, M. Chondrules as direct thermochemical sensors of solar protoplanetary disk gas. *Science Advances* **4**, 1–12 (2018).
30. Fendrich, K. V. & Ebel, D. S. Comparison of the Murchison CM2 and Allende CV3 chondrites. *Meteoritics and Planetary Science* **56**, 77–95 (2021).
31. Huss, G. R., Alexander, C. M. O., Palme, H., Bland, P. A. & Wasson, J.T. Genetic Relationships between Chondrules, Fine-grained Rims, and Interchondrule Matrix. in *Chondrites and the Protoplanetary Disk* vol. 341 701 (San Francisco: Astronomical Society of the Pacific, Kaua'i, Hawai'i, 2005).
32. Hezel, D. C. & Palme, H. The chemical relationship between chondrules and matrix and the chondrule matrix complementarity. *Earth and Planetary Science Letters* **294**, 85–93 (2010).
33. Ushikubo, T., Kimura, M., Kita, N. T. & Valley, J. W. Primordial oxygen isotope reservoirs of the solar nebula recorded in chondrules in Acfer 094 carbonaceous chondrite. *Geochimica et Cosmochimica Acta* **90**, 242–264 (2012).
34. Jones, R. H. Relict grains in chondrules: Evidence for chondrule recycling. in *Chondrules and the Protoplanetary Disk* 163–172 (Cambridge University Press, Cambridge, 2011).
35. Ruzicka, A., Floss, C. & Hutson, M. Relict olivine grains, chondrule recycling, and implications for the chemical, thermal, and mechanical processing of nebular materials. *Geochimica et Cosmochimica Acta* **72**, 5530–5557 (2008).

36. Harju, E. R. *et al.* Progressive aqueous alteration of CR carbonaceous chondrites. *Geochimica et Cosmochimica Acta* **139**, 267–292 (2014).
37. Zolensky, M., Nakamura, T., Martinez, J. & Enokido, Y. An unusual porous, cryptocrystalline forsterite chondrule in Murchison. *Meteoritics & Planetary Science* **56**, 56–60 (2021).
38. Ruzicka, A. M., Hugo, R. C., Friedrich, J. M. & Ream, M. T. Accretion of warm chondrules in weakly metamorphosed ordinary chondrites and their subsequent reprocessing. *Geochimica et Cosmochimica Acta* **378**, 1–35 (2024).
39. Connolly, H. C. & Hewins, R. H. Chondrules as products of dust collisions with totally molten droplets within a dust-rich nebular environment: An experimental investigation. *Geochemica et Cosmochimica Acta* **59**, 3231–3246 (1995).
40. Forster, B., Van De Ville, D., Berent, J., Sage, D. & Unser, M. Complex wavelets for extended depth-of-field: a new method for the fusion of multichannel microscopy images. *Microscopy Research and Technique* **65**, 33–42 (2004).
41. Ahrens, J., Geveci, B. & Law, C. ParaView: An end-user tool for large-data visualization. in *Visualization Handbook* 717–731 (Elsevier, 2005). doi:10.1016/B978-012387582-2/50038-1.
42. Nguyen, A. N., Nakamura-Messenger, K., Keller, L. P. & Messenger, S. Diverse assemblage of presolar and solar system materials in anhydrous interplanetary dust particles: Coordinated NanoSIMS and TEM analyses. *Geochimica et Cosmochimica Acta* **336**, 131–149 (2022).
43. Chaumard, N., Defouilloy, C. & Kita, N. T. Oxygen isotope systematics of chondrules in the Murchison CM2 chondrite and implications for the CO-CM relationship. *Geochimica et Cosmochimica Acta* **228**, 220–242 (2018).
44. Chaussidon, M., Libourel, G. & Krot, A. N. Oxygen isotopic constraints on the origin of magnesian chondrules and on the gaseous reservoirs in the early Solar System. *Geochimica et Cosmochimica Acta* **72**, 1924–1938 (2008).
45. Hertwig, A. T., Kimura, M., Defouilloy, C. & Kita, N. T. Oxygen isotope systematics of chondrule olivine, pyroxene, and plagioclase in one of the most pristine CV3Red chondrites (Northwest Africa 8613). *Meteoritics and Planetary Science* **54**, 2666–2685 (2019).

46. Krot, A. N., Doyle, P. M., Nagashima, K., Dobrica, E. & Petaev, M. I. Mineralogy, petrology, and oxygen-isotope compositions of magnetite ± fayalite assemblages in CO3, CV3, and LL3 chondrites. *Meteoritics and Planetary Science* **57**, 392–428 (2022).
47. Jones, R. H., Saxton, J. M., Lyon, I. C. & Turner, G. Oxygen isotopes in chondrule olivine and isolated olivine grains from the CO3 chondrite Allan Hills A77307. *Meteoritics and Planetary Science* **35**, 849–857 (2000).
48. Ushikubo, T. & Kimura, M. Oxygen-isotope systematics of chondrules and olivine fragments from Tagish Lake C2 chondrite: Implications of chondrule-forming regions in protoplanetary disk. *Geochimica et Cosmochimica Acta* **293**, 328–343 (2021).
49. Nakashima, D. *et al.* Oxygen isotopes in crystalline silicates of comet Wild 2: A comparison of oxygen isotope systematics between Wild 2 particles and chondritic materials. *Earth and Planetary Science Letters* **357–358**, 355–365 (2012).
50. Matsuo, N. New mineral akaganeite, β-FeOOH, from Akagane Mine, Iwate Prefecture, Japan. J. Jpn. Assn. Mineral. Petrol. Econ. Geol. 59, 143–151 (1968). doi: 10.2465/ganko1941.59.143. *The Journal of the Japanese Association of Mineralogists, Petrologists and Economic Geologists* **59**, 143–151 (1968).
51. Cornell, R. M. & Schwertmann, U. *The Iron Oxides: Structure, Properties, Reactions, Occurrence and Uses, 2nd, Completely Revised and Extended Edition*. (Wiley and Sons, Hoboken, N. J., 2006).
52. Grossman, J. N., Alexander, C. M. O. D., Wang, J. & Brearley, A. J. Zoned chondrules in Semarkona: Evidence for high-and low-temperature processing. *Meteoritics and Planetary Science* **37**, 49–73 (2002).
53. Marrocchi, Y. *et al.* Isotopic evidence for two chondrule generations in CR chondrites and their relationships to other carbonaceous chondrites. *Earth and Planetary Science Letters* **593**, 117683 (2022).

Acknowledgments

This material is based upon work supported by NASA under Contract NNM10AA11C issued through the New Frontiers Program. We acknowledge the entire OSIRIS-REx team for enabling Bennu sample return and analysis. We thank the Astromaterials Acquisition and Curation Office,

part of the Astromaterials Research and Exploration Science Division at Johnson Space Center, for their efforts in sample recovery, preliminary examination and long-term curation. We thank C.W.V. Wolner for constructive comments and valuable guidance during manuscript preparation.

Author Contributions

K.T.-K and L.L. conceived this study. K.T.-K., L.L., S. C., L.B.S., L.P.K., A.N.N., R. H. R. H. Z. R., T.E., L.S. and J. G. participated in sample selection, data collection and data analyses for this study. K.T.-K., L.L., S. C., L.B.S., L.P.K., A.N.N., R.H., T.E., T.J.M., T.J.Z., S.S. R., H.C.C. and D.S.L. contributed to discussions, text revisions, and manuscript reviews. The draft manuscript was compiled by K.T.-K. who was also responsible for final revisions.

Data Availability

The instrument data products underlying the findings of this work will be available via AstroMat at the DOIs given in Supplementary Data Table 7.

Methods

Seven Bennu particles were characterized for this study:

OREX-803437-100 is a fine-sized particle (~ 0.08 mm^3) sub-sampled from aggregate sample OREX-800070-0 with a mass of 74 g. The parent sample of OREX-800070-0 is OREX-800012-0, which had a collective mass of 25596 g. A FIB section, OREX-800070-104, was extracted from OREX-803437-100.

OREX-803079-241 is an intermediate-sized particle (~ 0.2 mm^3) from OREX-803079-0, which is a sub-sample from OREX-803017-0 with a mass of 47 g. Two FIB sections, OREX-803079-100 and OREX-803079-101, were extracted from OREX-803079-241.

Coarse-sized particles included: OREX-803417-103, ~ 1.5 mm in length (parent sample OREX-800068-0); OREX-803429-100, ~ 0.65 mm in length (parent sample OREX-803429-0); OREX-803434-100, ~ 1 mm in length (parent sample OREX-803434-0); OREX-803395-103, ~ 1 mm in length (parent sample OREX-803395-0); and OREX-803428-100,~ 1.3 mm in length, (parent sample OREX-803428-0).

Sample Preparation and Analysis Sequence

The overall analysis sequence for each particle followed different paths and so are summarized separately.

OREX-803437-100 Analysis Sequence

- Attached to an Al cylinder specimen mount using double-sided conductive adhesive tape
    - Optical and SEM (backscatter electron (BSE) imaging, secondary electron imaging (SEI), and energy dispersive X-ray (EDX) analyses
- Removed from the Al cylinder mount, epoxy-embedded and dry-polished to create a petrographic section
    - Reattached to Al cylinder mount using double-sided conductive adhesive tape
    - Optical and SEM (BSE, SEI, EDX and electron backscatter diffraction (EBSD) analyses

OREX-803079-241 Analysis Sequence

- Attached to an Al cylinder specimen mount using double-sided conductive adhesive tape

- Topside -- Optical and SEM (BSE, SEI, and EDX) analyses
- Two TEM sections extracted and welded to Cu FIB lift-out grids
    - TEM analysis

- Removed from the cylinder mount and placed in a polyethylene sample holder
    - X-ray computed tomography (XCT) analysis
- Reattached to an Al cylinder mount using double-sided conductive adhesive tape
    - Underside -- Optical and SEM (BSE, SEI, and EDX) analyses
- Removed from the Al cylinder mount, epoxy-embedded and dry-polished to create a petrographic section
    - Reattached to an Al cylinder mount using double-sided conductive adhesive tape
    - Optical and SEM (BSE, SEI, EDX and EBSED) analyses

OREX-803417-103 Analysis Sequence

- Attached to an Al cylinder specimen mount using double-sided conductive adhesive tape
    - Topside -- Optical and SEM (BSE, SEI, and EDX) analyses
    - Underside -- Optical and SEM (BSE, SEI, and EDX) analyses
- Removed from the cylinder mount and placed in a polyethylene sample holder
    - XCT analysis

OREX-803429-100, OREX-803434-100, OREX-803395-103, OREX-809428-100 Analysis Sequence

- Each particle was attached to an Al cylinder specimen mount using double-sided conductive adhesive tape
    - Optical and SEM (BSE, SEI, and EDX) analyses

Analytical Techniques

Optical Microscopy

Optical images were acquired using a Nikon BX-60 microscope at NASA Johnson Space Center (JSC). Since the topographic relief of the sample surfaces exceeded the imaging depth of focus at any useful objective magnification, it was necessary for each field of view to acquire image stacks covering the full focus range (typically 20–30 images) with could then be subsequently combined using a complex-wavelet algorithm[40] to generate a single in-focus image with an extended depth

of field. Multiple such images could then be stitched together to create mosaics with a larger field of view.

Field Emission Scanning Electron Microscopy/Electron Backscatter Diffraction

At NASA JSC, samples OREX-803437-100 and OREX-803079-241 were attached to an Al cylinder SEM mount using double-sided C tape. Following initial documentation by optical imaging, samples were sputter-coated with ~15 nm of conductive C to assist with charge dissipation using SEM analysis. Imaging of rough particles was accomplished using JEOL 7600F and 7900F FESEMs at accelerating voltages of 5, 10 and 15 kV using secondary electron and backscatter electron modes. Particles were analyzed at 15 kV and ~ 900 pA in high vacuum using an Oxford Instruments large-area (170 mm^2) silicon drift Ultim Max EDX detector. Both 1D (EDX point spectra) and 2D (EDX element maps) were acquired using Oxford AZtec 'Point & ID' and 'Mapping' software. For point analyses, acquisition times ranged from 20 to 200 s; for EDX mapping (1,024 × 768 pixels), dwell times of 400 ms/pixel were used with up to 5 frame accumulations. EDX data reduction was done with factory-installed standards, with the processing option for oxygen based on stoichiometry and results normalized.

Microstructural analysis and determination of crystallographic orientation was performed using a JEOL 7900F SEM, equipped with an Oxford Symmetry EBSD detector and a Zeiss Gemini 560 SEM with a Bruker E Flash FS EBSD detector. A Hitachi ArBlade 5000 broad beam Ar^+ ion milling system was first used to prepare uniformly flat sample surfaces. For EBSD analysis, samples were mounted on a pre-tilted holder set at an angle of 70° and analyzed using an accelerating voltage of 20 kV.

Electron Microprobe

Electron microprobe analysis was conducted on a C-coated, polished section of OREX-803079-241 at NASA JSC using a JEOL 8530-FE Electron Probe Microanalyzer (EPMA). Well-established standards were used for olivine analyses with collection parameters of 15 kV accelerating voltage and 20 nA beam current using a beam spot size of ~1 µm. Standards for microprobe analysis include Springwater Olivine (Smithsonian USNM 256) for Mg and Si; Sitkin Anorthite (Smithsonian NMNH 137041) for Al; Diopside (SPI minerals) for Ca; Chromium (III) oxide (SPI Minerals ZAS2070) for Cr; Rhodonite (SPI Minerals ZAS1320) for Mn; Rutile (SPI

Minerals ZAS6390) for Ti; and, Rockport fayalite (Smithsonian NMHM 85276) for Fe. The rhodonite and chromium (III) oxide standards were also used to account for the $Cr_{K\alpha}$ interference on the $Mn_{K\alpha}$ peak. Locations of point analyses and comparison of element abundances acquired by EPMA-WDS and SEM-EDX are shown in Supplementary Data 1.

X-Ray Computed Tomography

XCT was performed using the Zeiss 620 Versa instrument at the High-Resolution X-ray Computed Tomography Facility at the University of Texas at Austin (UTCT). Scanning was performed using a 90kV X-ray source at 12 watts with a LEI filter. Two volumes of 3701 views were collected (10 s. acquisition time per view) and stitched together for the final tomographic volume. The data were reconstructed into 16-bit TIFF images using a beam hardening correction of 2.25 and a voxel size of 0.9581 μm^3 using the Zeiss Xradia Reconstructor software package. Volumetric rendering and image analysis were performed using the open source ParaView[41] post-processing visualization engine.

Focused Ion Beam Microscopy

At NASA JSC, electron transparent FIB sections for TEM analysis were extracted using an FEI Quanta3D field emission gun FIB-SEM microscope. Prior to FIB extraction, a thick C protective strap (~ 500–1200 nm) was deposited over the section to protect it during subsequent ion milling. Ion milling was initially performed using a 30 kV Ga^+ beam at 3 nA current; this was reduced in a stepwise fashion as section preparation neared completion to reduce sample damage and milling artifacts. Thin sections, ~ 400 nm thick, were lifted out *in situ* using an Omniprobe 200 micromanipulator and welded to a Cu crescent TEM grid. These were then gradually polished down to ~ 80–100 nm using a 10 pA Ga^+ beam current to reduce curtaining due to differential milling and Ga surface implantation.

Scanning Transmission Electron Microscopy

Imaging by STEM was performed at NASA JSC using a JEOL 2500SE TEM operated at 200 kV equipped with a Gatan Digiscan system for bright-field and dark-field STEM imaging and a OneView 4 k × 4 k pixel CMOS camera for high-resolution TEM imaging and selected area electron diffraction (SAED). EDX analyses, including semi-quantitative X-ray point spectra and element

maps, were acquired with a JEOL (60 mm^2), thin window silicon drift detector. Element maps were acquired with a 4 nm diameter incident probe and a dwell time of 50 μs/pixel. Each pixel contains high count EDX spectra sufficient to provide better than 1 % counting statistics to determine major elemental abundances (multiple pixels are summed to define a region of interest) and their spatial distributions. Bright-field TEM images and SAED patterns were acquired from regions of interest. Diffraction patterns were processed using Gatan Digital Micrograph® and ImageJ and compared with simulated electron diffraction patterns calculated using the SingleCrystal™ software package.

Nanoscale Secondary Ion Mass Spectrometry

The CAMECA NanoSIMS 50L at NASA JSC was used to concurrently analyze oxygen isotopes of chondrule olivine in particles OREX-803437-100 and OREX-803079-241. Well-established analytical protocols were implemented for sample analysis[42]. Prior to analysis, the region was first sputtered using a ~ 250 pA Cs^+ beam to clean the surface and allow the secondary ion count rates to reach a steady state. Isotopic analyses were performed on a polished surface of a chondrule fragment in OREX-803437-100 (see Fig. 1b) and an interior chondrule fragment in OREX 803079-241 (see Fig. 5a). Using a 100 nm diameter Cs^+ beam with a current of 1−2 pA, three rastered areas of olivine from each chondrule fragment were analyzed. Areas ranged in size from 25 × 25 μm^2 to 32 × 32 μm^2 with a pixel size from 0.097668 to 0.11716 μm/px. An electron flood gun was used to mitigate sample surface charging and a nuclear magnetic resonance (NMR) B-field probe for maintaining the magnetic field stability to within 1 ppm. Dwell times ranged from 1000–2000 μs per pixel and 50–80 successive image frames were acquired for a given analysis region. Data processing was performed using L'image software (developed by Professor Larry Nittler, School of Earth and Space Exploration at Arizona State University) with corrections made for detector dead time, quasi-simultaneous ion arrival, and image drift.

Figures

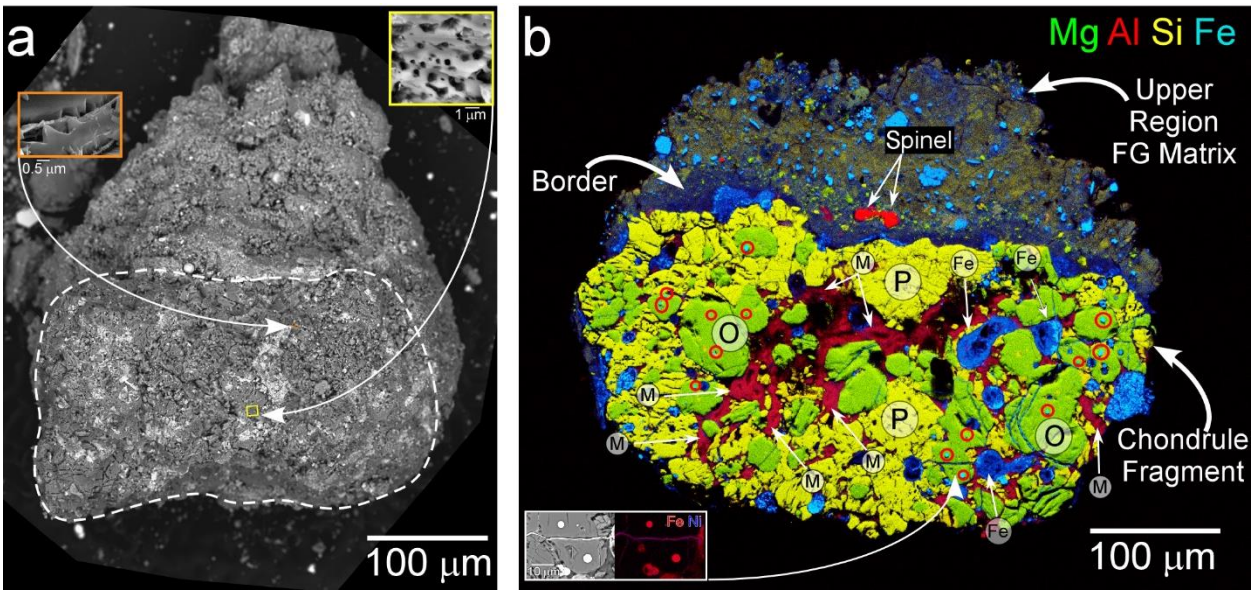


Figure 1. Texture, Composition and Mineralogy of a POP Chondrule Fragment in OREX-803437-100: (a) FESEM low angle backscatter electron (LABE) image of triangular-shaped particle OREX-803437-100 composed of fine-grained matrix (upper region) and a chondrule fragment outlined by the white dashed line (lower region). Aqueous alteration of pyroxene is shown by sawtooth features and diamond-shaped pits in the left and right insets, respectively. **(b)** Multi-element map of a polished surface of particle OREX-803437-100 containing fine-grained matrix (upper region) and a chondrule fragment (lower region). Adjacent to the fragment is a thin border region enriched in Na. The fine-grained matrix contains Mg-spinels (red). The chondrule fragment is composed of Mg-rich olivine (green; 'O'), low-Ca, Mg-rich pyroxene (yellow; 'P'), a Mg-rich secondary phase (dark fuchsia; 'M'), an Fe-rich secondary phase (deep blue; 'Fe'), magnetite and Fe-sulfides (light blue), and Fe-Ni metal hotspots (cyan; highlighted by red circles, embedded in olivine). Inset at lower left shows a magnified LABE view of two rounded Fe-Ni hotspots (location on the map, indicated by the white arrow) and a corresponding multi-element map of Fe (red) and Ni (blue).

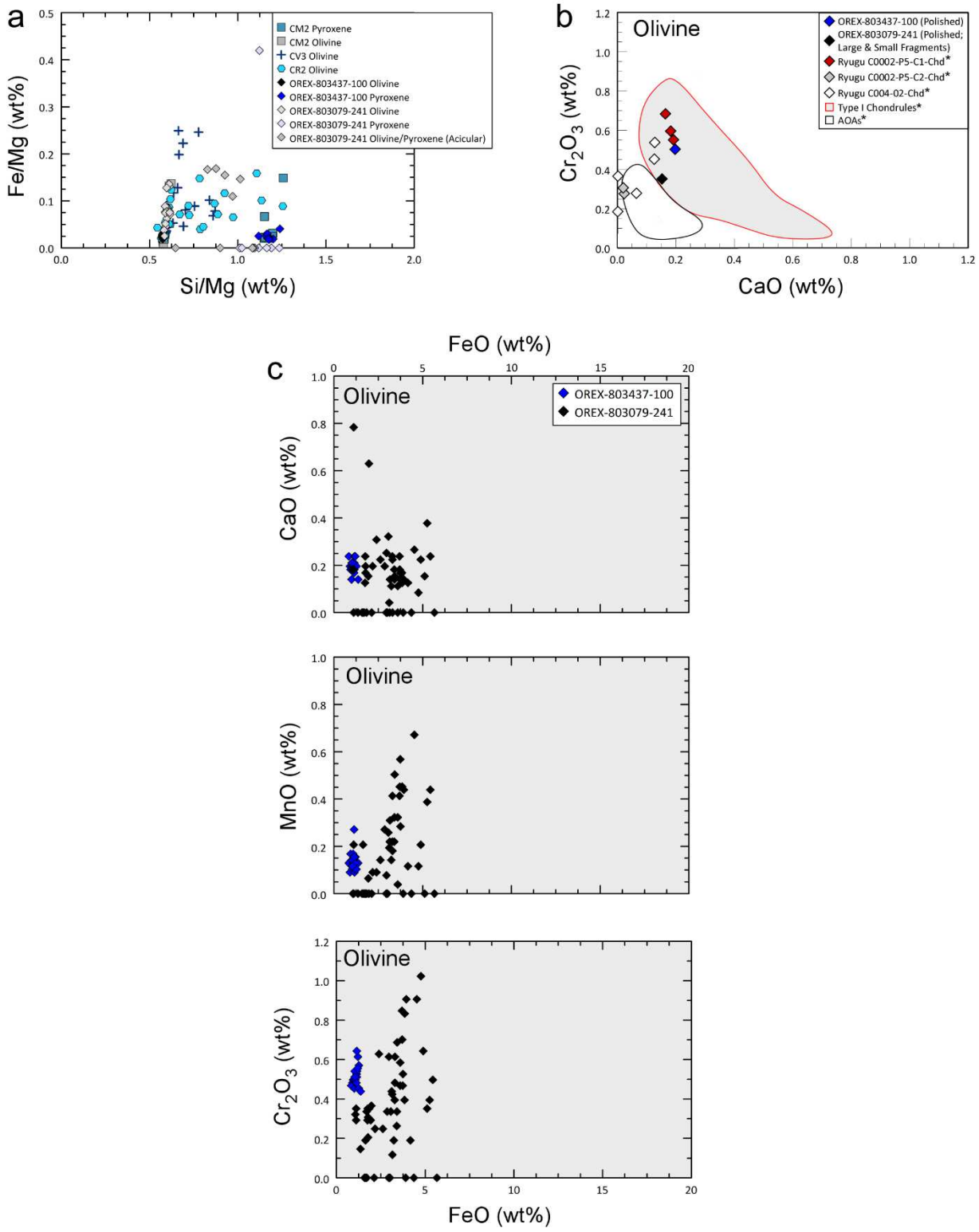


Figure 2. SEM-EDX Compositions of Olivine and Pyroxene in Chondrule Fragments in OREX-803437-100 and OREX-803079-241: (a) Si:Mg (wt%) versus Fe:Mg (wt%) for olivine and pyroxene in chondrule fragments in particles OREX-803437-100 and OREX-803-79-241. For comparison,

643 olivine and pyroxene data are shown for type I chondrules in petrologic grade ≤ 3.0 chondrites:
644 CM2[22] (Murray pyroxene and olivine); CV3[23] (Vigarano and NWA 3118 olivine); and CR2[23] (NWA
645 6043, NWA 801, and LAP 02342 olivine) (see Supplementary Data Table for Figure 2a). **(b)**
646 Average abundances of minor oxides CaO (wt%) versus Cr_2O_3 (wt%) in Mg-rich olivine from
647 polished chondrule fragments in particles OREX-803437-100 and OREX-803079-241. Olivine data
648 from three chondrule-like objects in Ryugu, type I chondrules in petrologic grade ≤ 3.0 chondrites,
649 and ameboid olivine aggregates (AOAs) are plotted for comparison (adapted from Nakashima et
650 al.[25], their Figure 4 and references therein; also see Supplementary Data for Tables 2 and 4). **(c)**
651 Minor oxide compositions of Mg-rich olivine in OREX-803437-100 and OREX-803079-241
652 chondrule fragments. Data for olivine in OREX-803437-100 appear localized, being from a single
653 porphyritic fragment. In comparison, data from OREX-803079-241 originate from two external
654 barred fragments and 20 barred fragments exposed on a polished surface (see Figs. 3 and 4a for
655 chondrule fragment locations; also see Supplementary Data for Tables 2-4). Values for Bennu
656 chondrule fragments overlap with those reported for olivine in type I chondrules in carbonaceous
657 chondrites [26–28].
658

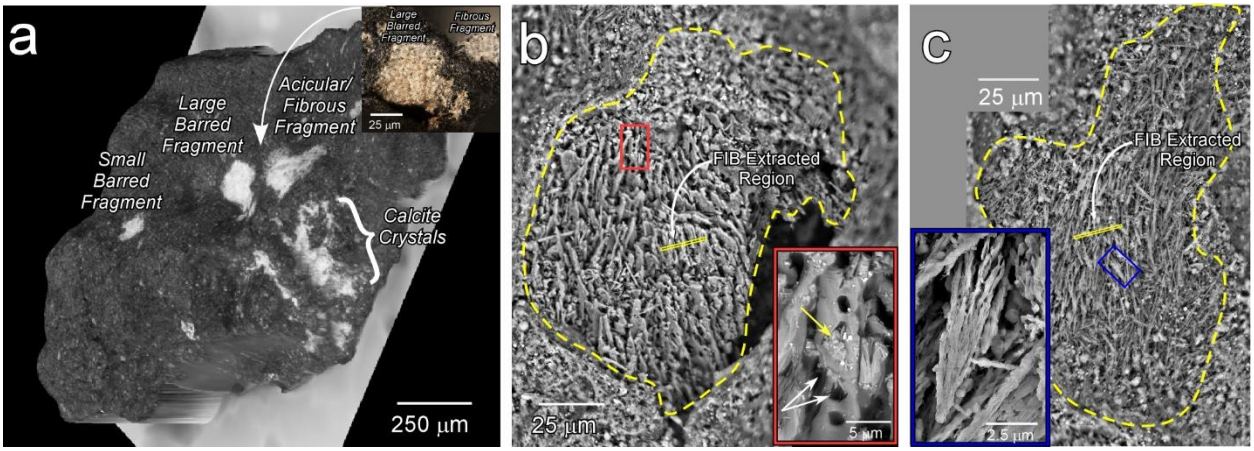
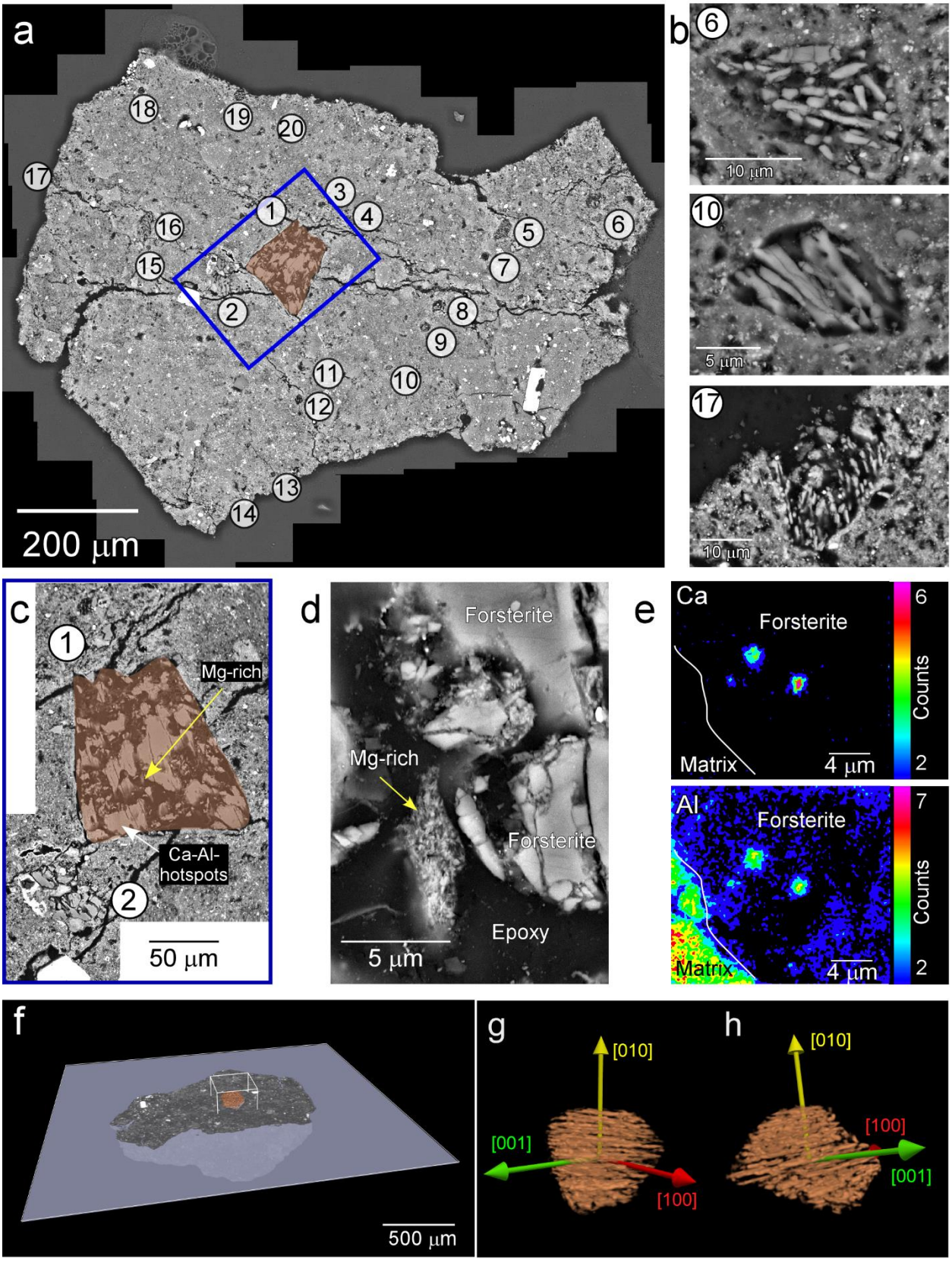


Figure 3. Texture of OREX-803079-241 BOP and RPO Chondrule Fragments: (a) Optical image of the topside of Bennu particle OREX-803079-241 containing light-colored chondrule fragments (labeled) that contrast with the underlying fine-grained matrix that appears gray to black in color. True color images show that the fragments are cream-colored, having a pale yellowish hue with some exhibiting a reddish-brown tint (inset, upper right). A collection of euhedral calcite crystals, ≤ 3 μm in size, cascades along the right side of the particle edge. **(b)** High-magnification FESEM LABE view (collected at 5 kV) of the large barred fragment in (a), outlined by a dashed yellow line. The area outlined by the red box is magnified in the inset at lower right. Siliceous crystals are arranged in stacks of semi-parallel plates of Mg-rich olivine and, to a lesser extent, low-Ca pyroxene. The region outlined by the yellow rectangle designates the location of a FIB extracted section. Plates often display perforated textures with pore sizes ranging from ~1 to 3 μm (inset; white arrows). Micron-sized regions of fine-grained matrix are commonly dispersed among the plates (inset; yellow arrow). The texture and composition of the small barred fragment in (a) is comparable to that shown here (see Extended Data Table 3). **(c)** High-magnification FESEM LABE view (collected at 5 kV) of the acicular/fibrous region in (a), outlined by a dashed yellow line. The area outlined by the blue box is magnified in the inset at lower left. Composed of acicular crystals of Mg-bearing olivine and low Ca-pyroxene with sub-micron diameters, some fibers have semi-parallel orientations while others converge to a single point (inset). The magnified LABE view shows pore space between siliceous fibers and micropores present within some fibers. The region outlined by the yellow rectangle designates the location of a FIB-extracted sample.


a
200 μm
b
6
10 μm
10
5 μm
17
10 μm
c
1
Mg-rich
Ca-Al-hotspots
2
50 μm
d
Forsterite
Mg-rich
Forsterite
Epoxy
5 μm
e
Ca
Forsterite
Matrix
4 μm
6
Counts
2
Al
Forsterite
Matrix
4 μm
7
Counts
2
f
500 μm
g
[010]
[001]
[100]
h
[010]
[100]
[001]

681

682 **Figure 4. Composition and Mineralogy of BOP Chondrule Fragments on an Internal Polished**
683 **Surface of Particle OREX-803079-241: (a)** FESEM LABE mosaic image of a polished, internal
684 surface of particle OREX-803079-241 containing a centrally located chondrule fragment (labeled
685 #1, false-colored orange). Before polishing, XCT imaging showed the fragment had a barred
686 texture (see Supplementary Data Videos 1 and 2). The irregular-shaped fragment is a direct
687 consequence of the angle at which it was polished. Additional barred fragments, labeled #2–20,
688 were also exposed at the polished surface. **(b)** Magnified FESEM LABE images of barred chondrule
689 fragments #6, #10, and #17 on the polished surface of particle OREX-803079-241. The smallest
690 fragment (#10) is ~ 10 μm in size. **(c)** High-magnification FESEM LABE image of fragments #1 and
691 #2 with an orange false-color overlay on #1. A Mg-rich region (yellow arrow) and a region
692 containing Ca-Al hotspots in Mg-rich olivine (white arrow) within the chondrule fragment are
693 shown in detail in (d) and (e), respectively. **(d)** High-magnification FESEM LABE image of a Mg-
694 rich region with a mottled texture (location given in (c), yellow arrow). Such regions are in pore
695 spaces between olivine and pyroxene grains. **(e)** Hue-saturation-intensity (HSI) element maps of
696 Ca and Al identifying hotspots containing both elements (location given in (c), white arrow). Each
697 hotspot is ~ 2 μm in size and embedded in a Mg-rich olivine grain in chondrule fragment #1. A
698 fine-grained phyllosilicate matrix (lower left) borders the fragment. **(f)** XCT reconstruction of
699 particle OREX-803079-241, which had been polished to reveal the centrally located barred
700 chondrule fragment (highlighted by an orange false-color overlay and a white box frame; also see
701 (a) and Supplementary Data Videos 1 and 2). **(g, h)** Magnified XCT reconstructions of the central
702 chondrule fragment revealing the nature and orientation of the siliceous bars. EBSD inverse pole
703 data (not shown) revealed that the siliceous bars are elongated along the crystallographic c-axis
704 [001] and orthogonal to the b-axis [010] of olivine.
705

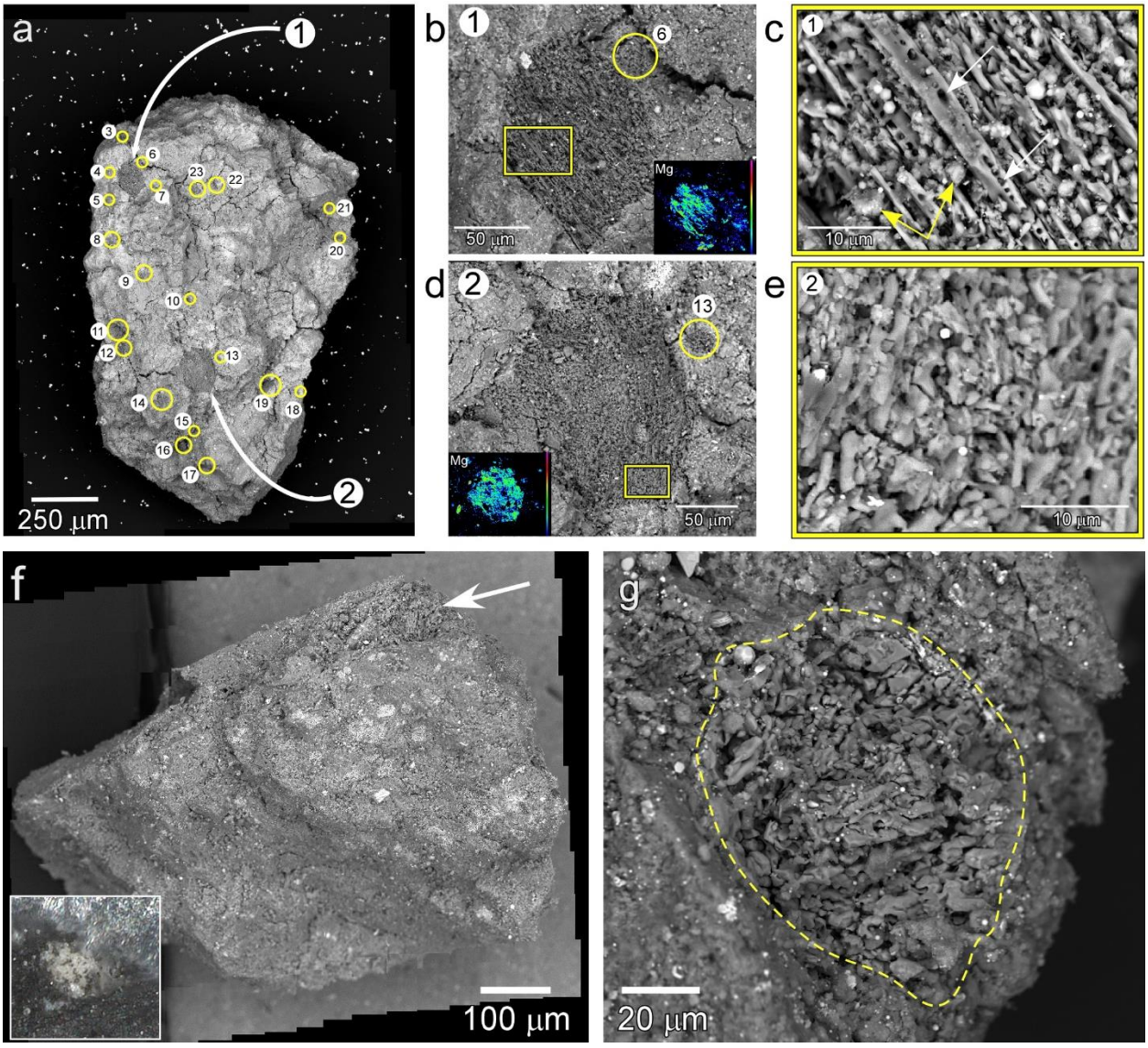


Figure 5. Location and Textures of BOP Chondrule Fragments in Particles OREX-803417-103 and OREX-803429-100: (a) FESEM LABE image of the topside of rectangular particle OREX-803417-103 that contains 23 chondrule fragments (outlined by yellow circles). **(b)** Higher-magnification FESEM LABE view of chondrule fragment #1 in OREX-803417-103 revealing a barred texture with a smaller barred fragment (#6) at upper right. The Mg element map, inset at lower right, indicates that the fragment is composed primarily of Mg-bearing olivine (also see Extended Data Table 5). The region outlined by the rectangle is magnified in (c). **(c)** Magnified view of a region of barred fragment #1 (see (b) for location) composed of stacks of semi-parallel plates of Mg-rich olivine and, to a lesser extent, low-Ca pyroxene. Plates often display perforated textures with pore sizes ranging from ~ 1–3 μm (white arrows). Micron-sized regions of fine-grained matrix are commonly

dispersed among the plates (yellow arrows). **(d)** Higher-magnification FESEM LABE view of chondrule fragment #2 in particle OREX-803417-103, revealing a choppy, barred texture with a smaller barred fragment (#13) near the upper right. The Mg element map, inset at lower left, indicates that the fragment is composed primarily of Mg-bearing olivine. The region outlined by the rectangle is magnified in (e). **(e)** Magnified view of a region of barred fragment #2 (see (d) for location) composed of broken semi-parallel plates of Mg-rich olivine and, to a lesser extent, low-Ca pyroxene. The appearance of the irregular-shaped silicate grains in this barred chondrule fragment is a direct consequence of the angle at which it is viewed. **(f)** FESEM LABE image of the topside of triangular particle OREX-803429-100 with the location of a single chondrule fragment, lower right, highlighted by a white arrow. Optical image of the fragment (inset, lower left) shows that it has a pale cream color. **(g)** High-magnification FESEM LABE view of the chondrule fragment in (f), outlined by a dashed yellow line, showing that it is composed primarily of sub-parallel fractured grains of Fe-bearing olivine with lesser Fe-bearing pyroxene (see Extended Data Table 5).

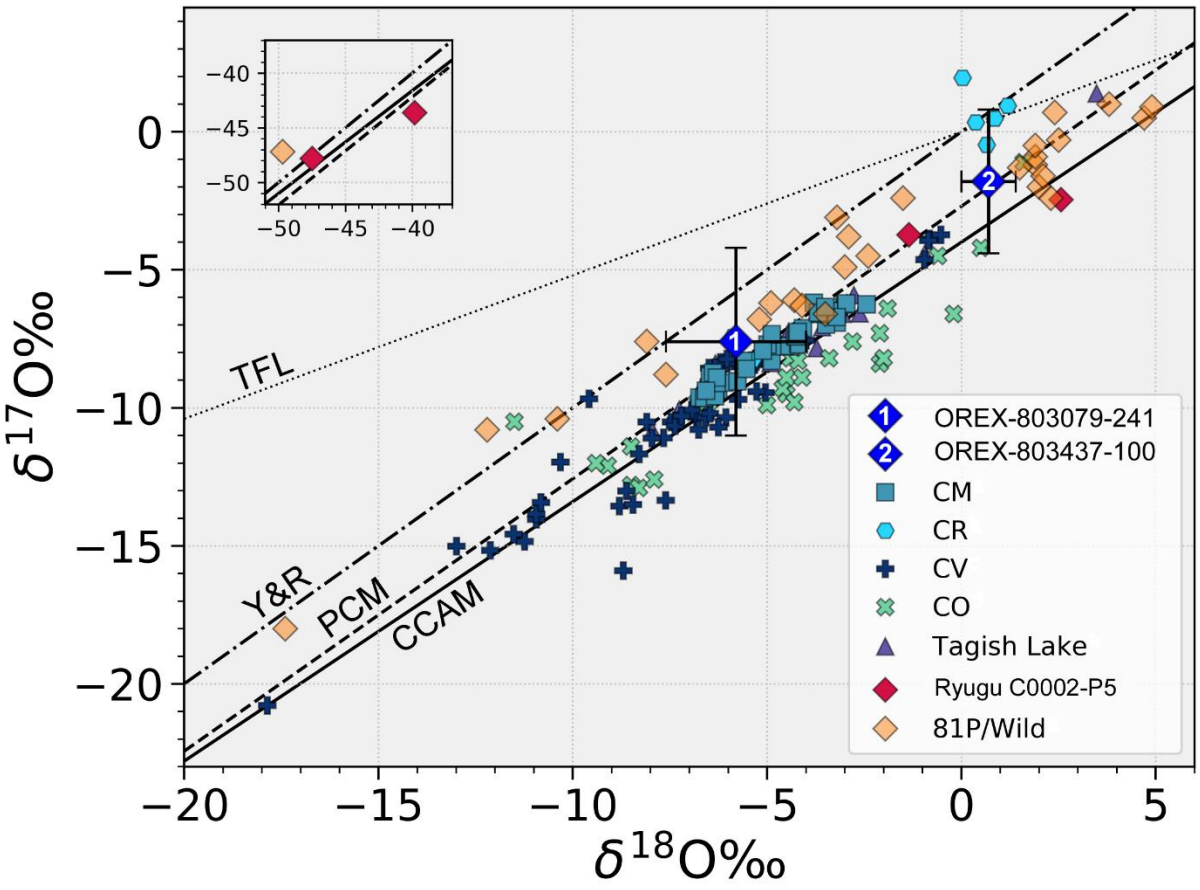
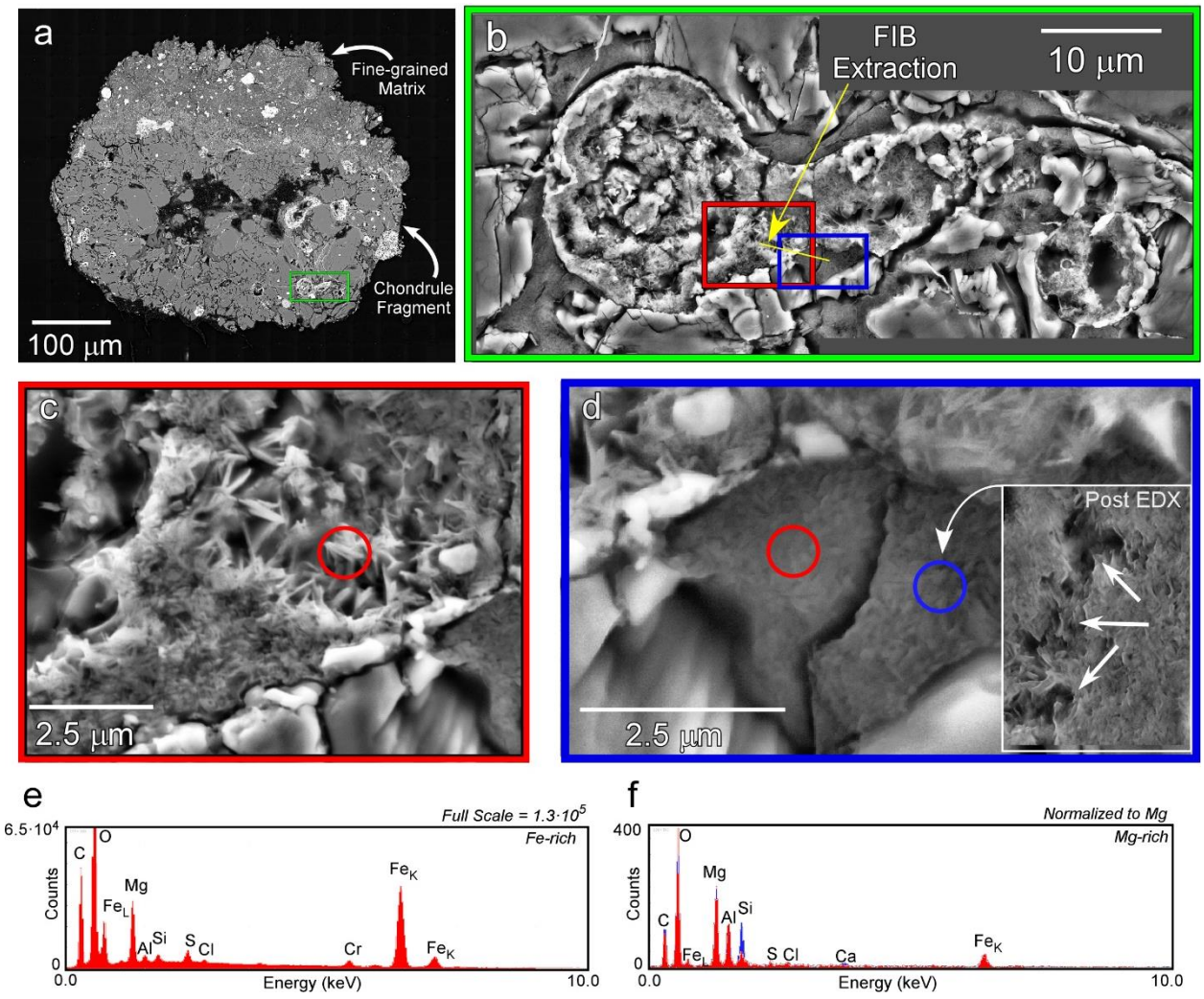


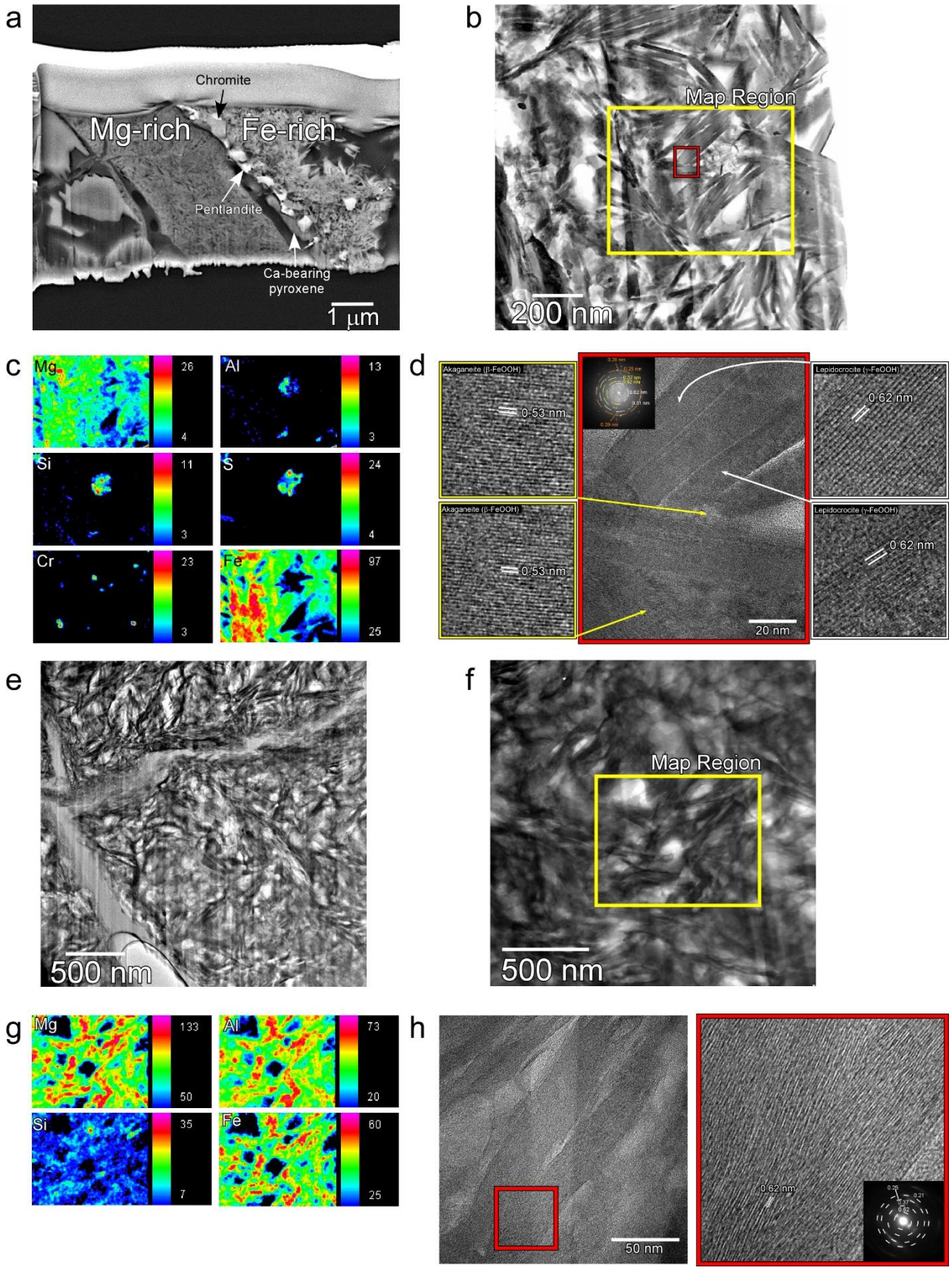
Figure 6. Oxygen Isotopic Ratios for Chondrule Olivine in OREX-803079-241 and OREX-803437-100: Bulk O isotopic ratios ($d^{18}O$: $d^{17}O$) of Mg-rich olivine in chondrule fragments in particles OREX-803437-100 and OREX-803079-241. Oxygen isotopic ratios for chondrule olivine in CM[43], CR[44], CV[44,45], CO[46,47], Tagish Lake (C ungrouped)[48] chondrites, Ryugu samples[25], and Comet 81P/Wild2[49] are shown for comparison (see Supplementary Data Table for Fig. 6). Reference lines: Terrestrial Fraction Line (TFL), Young and Russell line (Y&R), Primitive Chondrule Minerals line (PCM) and Carbonaceous Chondrite Anhydrous Mineral line (CCAM). The PCM line has slope 1 [$\delta^{17}O = (0.987 \pm 0.013), d^{18}O (2.70 \pm 0.11)$] and intersects the TFL at $\delta^{18}O = 5.8 \pm 0.4$.

Extended Data Figures



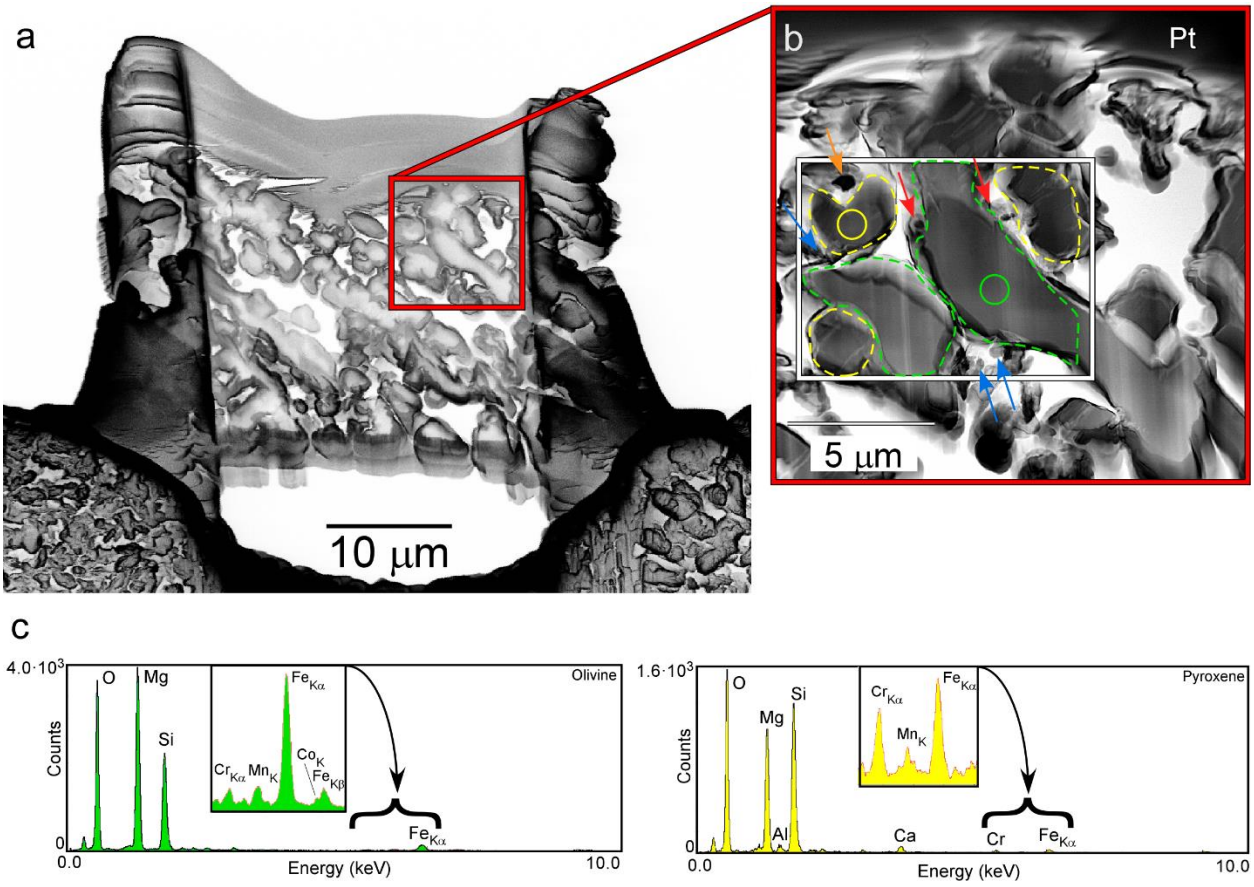
Extended Data Figure 1. Composition of Mg- and Fe-rich Secondary Phases in the POP Chondrule Fragment in OREX-803437-100: (a) FESEM LABE image of the polished surface of particle OREX-803437-100. The chondrule fragment is located in the lower region adjacent to the fine-grained phyllosilicate matrix (also see Fig. 1). A green rectangle highlights location of a region of interest (ROI) containing secondary Fe- and Mg-rich phases. **(b)** Magnified FESEM LABE image of the region outlined by the green rectangle in (a). This region has a pseudo-lemniscate shape with the location of a FIB-extracted section highlighted by the yellow arrow/line. Fe- and Mg-rich regions are outlined by the red and blue boxes and shown at higher magnification in (c) and (d), respectively. **(c)** Magnified FESEM LABE view of the Fe-rich phase (for location see (b)) composed

of acicular fibers. Location of the EDX point spectrum is shown by the red circle. **(d)** Magnified FESEM LABE view of the Mg-rich phase (for location see (b)) displaying a pseudo-fibrous surface texture. Red and blue circles indicate locations of EDX point spectra. Inset at lower right shows pits (white arrows) in the Mg-rich phase following EDX analysis produced by exposure to a focused 15 kV/1 nA electron beam. **(e)** EDX point spectrum of the Fe-rich fibrous phase in (c) also containing Mg, Al, Si, S, Cl and Cr (also see Extended Data Table 2). **(f)** Two overlapping EDX point spectra of the Mg-rich phase in (d). Red and blue spectra are color matched to circles in (d) designating analysis locations. Both spectra contain Mg, Al, Si, S, Cl, Ca, Cr and Fe. Si abundance varies significantly among analysis locations (also see Extended Data Table 2).


a
Chromite
Mg-rich
Fe-rich
Pentlandite
Ca-bearing pyroxene
1 μm
b
Map Region
200 nm
c
Mg
26
4
Al
13
3
Si
11
3
S
24
4
Cr
23
3
Fe
97
25
d
Akaganeite (β-FeOOH)
0.53 nm
Lepidocrocite (γ-FeOOH)
0.62 nm
20 nm
e
500 nm
f
Map Region
500 nm
g
Mg
133
50
Al
73
20
Si
35
7
Fe
60
25
h
50 nm
0.62 nm

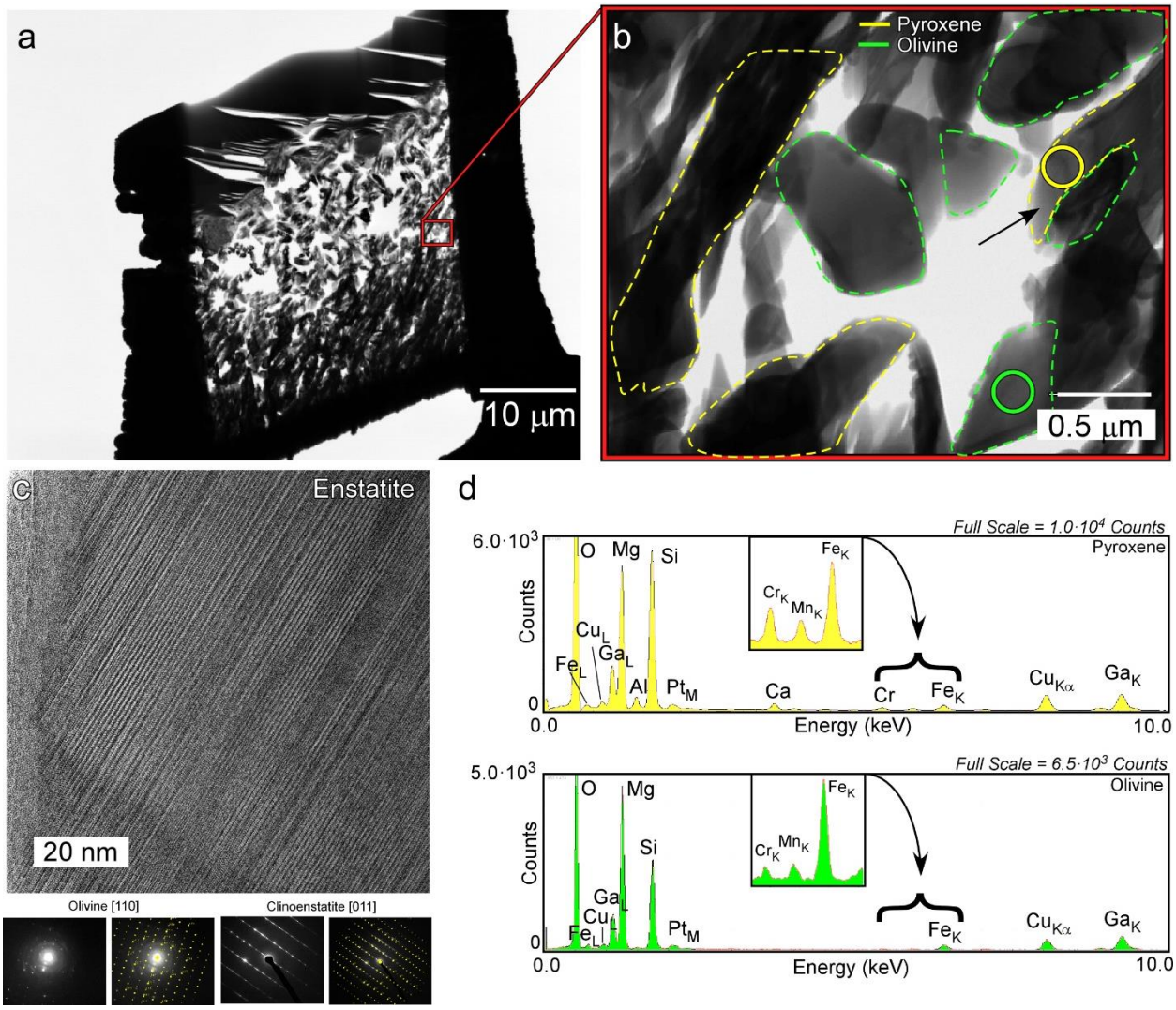
Extended Data Figure 2. Composition and Mineralogy of Mg- and Fe-rich Secondary Phases in a FIB Section Extracted from the POP Chondrule Fragment in OREX-803437-100: (a) FESEM backscatter image of a FIB thin section (OREX-800070-104; taken at 53°) extracted from the OREX-803437-100 chondrule fragment (see Extended Data Figure 1b for FIB extraction location). The section is composed of two distinct phases, with one being coarsely fibrous and Fe-rich (right) whereas the other is finely fibrous and Mg-rich (left). Crystals in contact with the two regions are composed of pentlandite, chromite and Ca-bearing pyroxene. **(b)** High-magnification bright-field TEM view of the Fe-rich phase composed of diverging fibers, some with radiating, fan-like shapes. Yellow box shows the location of accompanying TEM-EDX element maps in (c). Red box outlines the area shown at higher magnification in (d). **(c)** Hue-saturation-intensity (HSI) element maps of the Fe-rich fibrous phase showing the distribution of Mg, Al, Si, S, Cr and Fe (see (b) for location). The Fe-rich fibers contain major Mg with nanometer-sized clusters of fine-grained matrix (Al, Si, and S maps) and nanometer-sized chromite (Cr map) dispersed among the fibers (also see Extended Data Table 2). **(d)** High-resolution bright-field TEM image (outlined in red) of well crystalline, lath-shaped, Fe-rich fibers in the FIB extracted section (for location see (b)). Fast Fourier Transform (FFT) of this region (inset, upper left) shows overlapping patterns for akaganeite (d(nm) = 0.52, 0.37, 0.29, 0.25) and lepidocrocite (d(nm) = 0.62, 0.31, 0.29., 0.25) (note: spacing of 0.29 and 0.25 nm can correspond to either mineral). High-magnification TEM views of single direction lattice spacing on the left side of the central image correspond to akaganeite (0.53 nm lattice spacings) and on the right to lepidocrocite (0.62 nm lattice spacings). (Note: akaganeite and lepidocrocite can form as alteration (*e.g.*, oxidation/hydration) products of magnetite and pyrrhotite[50,51], minerals that are abundant in Bennu samples[15]). **(e, f)** Bright-field TEM images of the Mg-rich phase revealing its overall finely intertwined fibrous nature. Yellow box in (f) shows location of corresponding TEM-EDX element maps in (g). **(g)** HSI element maps of the Mg-rich region showing the distribution of Mg, Al, Si and Fe (see (f) for location), all present as major elements (see Extended Data Table 2). Several nanometer-sized hotspots of Si correspond to clusters of fine-grained phyllosilicate matrix intermingled with the Mg-rich fibers. Heterogenous distribution of Si is also observed by SEM-EDX (also see Extended Data Figure 1(f) and Extended Data Table 2). **(h)** High-magnification TEM view (left) of single direction lattice

794 spacings of the relatively poorly crystalline, Mg-rich fibrous phase. At right is a higher-
795 magnification TEM view of the region, outlined by the red box in the left view, showing lattice
796 spacings of ~ 0.62 nm. The SAED pattern (inset) shows diffuse, partial rings for diffraction spots
797 at 0.62, 0.37, 0.25 and 0.21 nm.
798



Extended Data Figure 3. Texture, Composition and Mineralogy of Phases in a FIB Section Extracted from a BOP Chondrule Fragment in OREX-803079-241: (a) Bright-field TEM image of the FIB section (OREX-803079-100) extracted near the center of the large barred feature on the topside of particle OREX-803079-241 (for location see Fig. 3(b), yellow rectangle). Region outlined by the red box is magnified in (b). **(b)** Bright-field TEM view of the outlined region in (a). Element maps were acquired for the area outlined by the white box (not shown) and indicate that the following minerals are present: low-Ca pyroxene (yellow dashed lines), Mg-rich olivine (green dashed lines), pyrrhotite (red arrows), chromite (blue arrows) and pentlandite (orange arrow). The FIB section is porous, lacking evidence of mesostasis or replacement phyllosilicate minerals. EDX point spectra locations for olivine and pyroxene are given by the green and yellow circles, respectively (see (c)). **(c)** TEM-EDX point spectra of Mg-rich olivine (green) and low Ca-pyroxene (yellow) (spectra locations given by the corresponding green and yellow circles in (b)). Mg-rich olivine contains major O, Mg, Si and Fe with minor Cr and Mn; a small peak on the side of the $Fe_{Kβ}$ peak suggests minor Co is present (inset). Low-Ca pyroxene contains major O, Mg, Si

and Al with minor Ca, and Cr (inset). In both spectra, the peak identified as Mn_K may also contain Cr (as Cr_{Kb}). Using SEM-EDX, these minor elements were not detected in pyroxene (Extended Data Table 3), suggesting either heterogenous compositions among crystals or elemental abundances of below detection levels.



Extended Data Figure 4. Texture, Composition and Mineralogy of Phases in a FIB Section Extracted from a RPO Chondrule Fragment in OREX-803079-241: (a) Bright-field TEM image of the FIB section (OREX-803079-101) extracted near the center of the acicular chondrule fragment on the upper surface of particle OREX-803079-241 (for location see Fig. 3c, yellow rectangle). The FIB section is porous, lacking evidence of mesostasis or replacement phyllosilicate minerals. Region outlined by the red box is magnified in (b). **(b)** Bright-field TEM view of the region outlined in (a) composed of Ca-poor pyroxene (yellow dashed lines) and Mg-rich olivine (green dashed lines). Black arrow designates location of a high-resolution TEM image shown in (c). Yellow and green circles show locations of EDX point spectra for pyroxene and olivine, respectively, shown in (d). **(c)** High-resolution TEM image of a pyroxene crystal composed of fine-scale intergrowths of clino- and ortho-enstatite polymorphs (for location see arrow in (b)). Below this view are SAED

831 images of forsteritic olivine [110] and clinoenstatite [011] from regions in (a), each accompanied
832 by the SAED image overlain by a simulated diffraction pattern corresponding to the appropriate
833 mineral zone axis. **(d)** TEM-EDX point spectra of low Ca-pyroxene (yellow) and Mg-rich olivine
834 (green) (spectra locations given by the yellow and green circles in (b)). In both spectra, the peak
835 identified as Mn_K may also contain Cr (as Cr_{Kb}) (see Extended Data Table 3).
836
837

Extended Data Tables

Extended Data Table 1: Location, Types and Abundances of Chondrule Fragments in Returned Bennu Samples

Particle Number	Particle Type	Chondrule Type	Number of Chondrule Fragments
OREX-803079-241	Hummocky	Barred olivine pyroxene (BOP), type I Radial pyroxene olivine, (RPO), type I	44* (9 outside, 35 inside)
OREX-803395-103	Angular	Barred olivine pyroxene (BOP), type I	2
OREX-803417-103	Hummocky	Barred olivine pyroxene (BOP), type I	41* (25 outside, 18 inside (2 internal fragments breached exterior surface))
OREX-803428-100	Angular	Barred olivine pyroxene (BOP), type I	1
OREX-803429-100	Hummocky	Barred olivine pyroxene (BOP), type II	1
OREX-803434-100	Hummocky	Barred olivine pyroxene (BOP), type I	1
OREX-803437-100	Hummocky	Porphyritic olivine pyroxene (POP), type I	1

*This represents fragments larger than ≥ 10 μm as smaller fragments are not included.

Extended Data Table 2: FESEM-EDX Composition of Phases in the OREX-803437-100 POP Chondrule Fragment and Surrounding Matrix

Elements (wt%) O by Stoichiometry	Olivine (22 ROI)	Low-Ca Pyroxene (15 ROI)	Ca-bearing Pyroxene (10 ROI)	Phyllosilicates assoc. with Pyroxene (3 ROI)	Mg-rich Phases (21 ROI)	Fe-rich Phases (8 ROI)	Fe-Ni Metal (8 ROIs)	Bulk Chondrule Large Analysis Region	Bulk Matrix Large Analysis Region	Bulk Chondrule + Matrix Large Analysis Region
O	45.1 ± 0.04	47.4 ± 0.05	45.3 ± 0.5	44.8 ± 0.5	38.8 ± 2.1	26.2 ± 0.9	n.d.	44.2	42.1	43.5
Na	n.d.	n.d.	n.d.	0.3 ± 0.1	0.2 ± 0.2	0.4 ± 0.2	n.d.	0.1	0.7	0.2
Mg	33.9 ± 0.08	23.2 ± 0.3	14.7 ± 2.2	20.4 ± 1.6	21.8 ± 2.3	9.1 ± 1.1	n.d.	25.1	12.9	21.4
Al	0.1 ± 0.02	0.5 ± 0.1	1.9 ± 0.5	2.6 ± 0.3	10.4 ± 2.8	0.3 ± 0.3	n.d.	1.1	1.3	1.1
Si	19.5 ± 0.05	27.3 ± 0.2	25.2 ± 0.5	22.6 ± 0.7	6.2 ± 4.4	0.3 ± 0.2	n.d.	19.7	14.1	17.6
S	n.d.	n.d.	n.d.	0.3 ± 0.1	1.2 ± 0.8	0.9 ± 0.4	n.d.	1.1	6.4	2.9
Cl	n.d.	n.d.	n.d.	0.2 ± 0.1	0.4 ± 0.2	0.1 ± 0.2	n.d.	0.1	0.4	0.2
Ca	0.1 ± 0.02	0.4 ± 0.06	11.3 ± 2.8	1.1 ± 0.2	0.4 ± 0.6	0.1 ± 0.1	n.d.	0.9	0.6	0.8
Ti	n.d.	0.1 ± 0.03	0.5 ± 0.2	0.1 ± 0.1	n.d.	n.d.	n.d.	0.1	n.d.	0.1
Cr	0.4 ± 0.03	0.3 ± 0.03	0.5 ± 0.3	0.9 ± 0.2	1.4 ± 0.3	0.6 ± 0.7	n.d.	0.5	0.4	0.5
Mn	0.1 ± 0.03	0.1 ± 0.02	0.1 ± 0.2	n.d.	0.0 ± 0.1	0.5 ± 0.3	n.d.	0.1	0.2	0.1
Fe	0.9 ± 0.1	0.6 ± 0.1	0.6 ± 0.1	6.7 ± 1.6	18.8 ± 5.9	61.1 ± 3.6	92.9 ± 2.1	6.0	19.1	10.2
Ni	n.d.	n.d.	n.d.	0.1 ± 1.0	0.5 ± 0.5	0.5 ± 0.4	7.1 ± 2.1	1.0	1.7	1.5
Mg/Si (wt%)	1.74	0.85	0.58	0.90	----	----	----	1.28	0.92	1.21
Reference Materials Mg/Si (wt%)	1.73 (Forsterite)	0.865 (Enstatite)	0.58[1] (Pigeonite)	0.97[1] (Antigorite)	----	----	---	Huss et al. (2005) fn. 2; Fendrich and Ebel (2021) fn.3; Hezel and Palme (2010) fn. 4	Huss et al. (2005) fn. 5 Hezel and Palme (2010) fn. 6	Hezel and Palme (2010) fn. 7

n.d. = not detected

[1] Standard from Webmineral (https://webmineral.com)
[2] Mg/Si = 1.03 ± 0.2 Renazzo (CR2) chondrules
[3] Mg/Si ~ 1.1 Murchison (CM2) bulk chondrules (see their Fig. 4)
[4] Mg/Si ~ 0.91 (mean) El-Quss Abu Said (CM2) bulk chondrules (see their Table A1)
[5] Mg/Si ~ 0.9 CI- & CM-bulk matrix and rims (see their Table 1)
[6] Mg/Si ~0.66-0.90 CM2 matrix; ~ 0.62-0.74 CR2 matrix
[7] Mg/Si ~0.90-0.91 CI-, CM-, & CR-bulk chondrites

Extended Data Table 3: FESEM-EDX Composition of Chondrule Fragments on the Topside of OREX-803079-241

Elements (wt%) O by Stoichiometry	Olivine Large Barred, Topside (10 ROI)	Low Ca-Pyroxene Large Barred, Topside (7 ROI)	Large Barred Fragment Topside (Bulk Analysis of Fragment ~2500 μm^2)	Olivine Small Barred, Topside (8 ROI)	Low Ca-Pyroxene Small Barred, Topside (4 ROI)	Small Barred Fragment Topside (Bulk Analysis of Fragment ~1500 μm^2)	Acicular Topside (8 ROI)	Acicular Topside (Bulk Analysis of Fragment ~1500 μm^2)	FG Matrix Topside & Underside (10 ROI)
O	45.5 ± 1.2	47.1 ± 1.0	44.2	45.1 ± 0.1	47.6 ± 0.3	44.6	46.1 ± 0.8	45.6	42.7 ± 0.5
Na	0.1 ± 0.1	0.1 ± 0.3	0.2	0.1 ± 0.1	n.d.	0.2	0.1 ± 0.3	0.3	1.5 ± 0.4
Mg	31.3 ± 1.0	23.6 ± 1.3	28.3	32.8 ± 0.6	25.1 ± 1.3	30.5	26.2 ± 3.0	23.3	12.6 ± 2.0
Al	0.3 ± 0.2	1.1 ± 0.9	0.8	0.1 ± 0.1	n.d.	0.4	1.2 ± 0.6	1.5	1.8 ± 0.3
Si	18.8 ± 0.6	26.3 ± 1.2	19.3	19.5 ± 0.3	27.3 ± 1.0	18.8	23.4 ± 1.7	22.4	15.4 ± 1.5
S	0.2 ± 0.1	n.d.	0.4	0.3 ± 0.2	n.d.	0.8	0.2 ± 0.4	0.9	6.0 ± 1.3
Ca	0.2 ± 0.1	0.5 ± 0.8	0.5	0.1 ± 0.1	n.d.	0.2	0.4 ± 0.6	0.8	0.3 ± 0.2
Cr	0.3 ± 0.1	n.d.	1.2	0.2 ± 0.1	n.d.	0.3	0.1 ± 0.2	0.5	0.4 ± 0.3
Mn	0.2 ± 0.1	n.d.	0.3	0.1 ± 0.1	n.d.	0.1	0.0 ± 0.1	0.3	0.0 ± 0.1
Fe	3.0 ± 0.7	1.3 ± 3.4	4.5	1.8 ± 0.6	n.d.	4.0	2.3 ± 2.0	4.2	18.5 ± 2.9
Ni	0.1 ± 0.1	n.d.	0.2	0.0 ± 0.1	n.d.	0.2	0.0 ± 0.1	0.2	0.9 ± 0.4
Mg/Si (wt%)	1.67	0.90	1.47	1.68	0.92	1.62	1.13	1.04	0.82
Mg/Si (wt%) Standards; Estimated Modal Abundances	1.73 (Forsterite)	0.87 (Enstatite)	~ 70% Forsterite + 30% Enstatite	1.73 (Forsterite)	0.87 (Enstatite)	~ 85% Forsterite + 15% Enstatite	~ 30% Forsterite + 70% Enstatite	~ 22% Forsterite + 78% Enstatite	~ 90% Phyllosilicates + Anhydrous Minerals

n.d. = not detected

Extended Data Table 4: FESEM-EDX Composition of Chondrule Fragments *within* OREX-803079-241
(Barred Fragments on Polished Surface*)

Elements (wt%) O by Stoichiometry	Olivine in Center Barred Fragment (#1) (12 ROI)	Low-Ca Pyroxene in Center Barred Fragment (#1) (8 ROI)	High-Ca Pyroxene in Center Barred Fragment (#1) (1 ROI)	Mg-rich Phases in Center Barred Fragment (#1) (6 ROI)	Small Barred Fragments (#2-20) (24 ROIs)
O	45.0 ± 0.1	47.4 ± 0.2	44.8	39.7 ± 1.3	44.8 ± 0.4
Na	n.d.	n.d.	n.d.	n.d.	n.d.
Mg	33.3 ± 0.8	23.2 ± 0.4	11.2	26.2 ± 1.5	31.6 ± 1.1
Al	0.3 ± 0.2	0.8 ± 0.4	5.8	5.8 ± 1.6	0.3 ± 0.2
Si	19.6± 0.2	27.1 ± 0.4	22.8	8.7 ± 3.0	20.0 ± 0.8
S	n.d.	n.d.	n.d.	0.3 ± 0.3	n.d.
Ca	0.1 ± 0.1	0.6 ± 0.3	13.2	0.0 ± 0.1	0.1 ± 0.1
Ti	n.d.	n.d.	n.d.	n.d.	n.d.
Cl	n.d.	n.d.	n.d.	n.d.	n.d.
Cr	0.2 ± 0.1	0.3 ± 0.1	0.7	7.0 ± 1.3	0.3 ± 0.2
Mn	n.d.	n.d.	0.7	n.d.	0.2 ± 0.2
Fe	1.5 ± 0.3	0.7 ± 0.3	n.d.	12.2 ± 3.0	2.7 ± 0.9
Ni	n.d.	n.d.	n.d.	n.d.	n.d.
Mg/Si (wt%)	1.70	0.86	0.49	----	1.59
Reference Standards Mg/Si (wt%)	1.73 (Forsterite)	0.87 (Enstatite)	0.46 (Augite $Na_{0.1}Ca_{0.9}MgFe_{0.1}Al_{0.4}Ti_{0.1}Si_{1.9}O_6$)		~ 80% Forsterite + ~20% Enstatite

n.d. = not detected
*See Figure 4

Extended Data Table 5: FESEM-EDX Composition of Chondrule Fragments in Particles OREX-803417-103 and OREX-803429-100

Elements (wt%) O by Stoichiometry	OREX-803417 Olivine (53 ROI)	OREX-803417 Pyroxene (22 ROI)	OREX-803417 Mg-rich Phases (14 ROI)	OREX-803429 Olivine (21 ROI)	OREX-803429 Pyroxene (5 ROI)
O	44.9 ± 0.4	47.0 ± 0.8	40.3 ± 1.1	41.2 ± 1.9	43.8 ± 0.2
Na	0.0 ± 0.1	n.d.	n.d.	n.d.	n.d.
Mg	31.8 ± 1.2	22.3 ± 1.5	24.6 ± 2.2	22.0 ± 1.6	16.8 ± 1.1
Al	0.6 ± 0.5	1.5 ± 1.5	9.1 ± 1.6	0.4 ± 0.5	2.0 ± 0.3
Si	19.4 ± 0.9	25.6 ± 1.7	9.6 ± 1.8	17.2 ± 0.8	23.4 ± 0.4
S	0.2 ± 0.2	0.2 ± 0.3	0.2 ± 0.2	0.1 ± 0.1	0.1 ± 0.1
Cl	n.d.	n.d.	n.d.	n.d.	n.d.
Ca	0.1 ± 0.1	1.0 ± 1.0	0.2 ± 0.3	0.1 ± 0.1	1.5 ± 0.2
Ti	n.d.	n.d.	n.d.	n.d.	0.0 ± 0.1
Cr	0.3 ± 0.2	0.5 ± 0.2	0.9 ± 1.1	0.2 ± 0.2	0.4 ± 0.4
Mn	0.2 ± 0.1	0.2 ± 0.2	0.1 ± 0.1	0.1 ± 0.1	0.1 ± 0.1
Fe	2.5 ± 1.1	1.9 ± 1.2	15.0 ± 2.8	18.9 ± 2.9	11.8 ± 1.0
Ni	n.d.	n.d.	n.d.	n.d.	n.d.
Mg/Si (wt%)	1.64	0.87	-----	1.28	0.72
Reference Standards Mg/Si (wt%)	1.73 (Forsterite)	0.87 (Enstatite)		1.30 (Fayalitic Olivine $Mg_{1.5}Fe_{0.5}SiO_4$)	0.65 (Ferrosillite $Mg_{1.5}Fe_{0.5}Si_2O_6$)

n.d. = not detected

Extended Data Table 6: Comparison of Bennu Chondrule Fragments to Chondrules in Carbonaceous Chondrites

Chondrule Class:	***Porphyritic Olivine Pyroxene***	**Bennu Particle**:	***OREX-803437-100***
Comparison to CC's	• Equant crystals of Mg-rich olivine and Mg-rich, low-Ca pyroxene as found in POP chondrules[1–10] • Major/minor element abundances within range of type I chondrules in primitive carbonaceous chondrites[11–13] • Fe-Ni metal inclusions as observed in porphyritic chondrules[14] • O isotopic composition within the range observed for chondrule olivine in carbonaceous chondrites (see Fig. 6 and references therein)		

Chondrule Class:	***Nonporphyritic*** ***Barred Olivine Pyroxene***	**Bennu Particles:**	***OREX-803079-241*** ***OREX-803417-103***
Comparison to CC's	• Semi-parallel spaced olivine laminae with smooth edges identical to BO chondrules [15,16] • Olivine b-axis [010] parallel to axis of stacking as observed in BO chondrules[17] • Major/minor element abundances in range of CM2[12], CV3[13] and CR2[12] chondrules • O isotopic composition in the range defined by Mg-rich chondrule olivine in primitive carbonaceous chondrites (see Fig. 6 and references therein)		

Chondrule Class:	***Nonporphyritic*** ***Radial Pyroxene Olivine***	**Bennu Particle:**	***OREX-803079-241***
Comparison to CC's	• Fibrous crystals of Mg-rich, low-Ca pyroxene and Mg-rich olivine with minor element compositions in range of bulk chondrules in carbonaceous chondrites[1,18,19]		

Extended Data References

1. Zolensky, M. E. *et al.* Chapter 2 - Physical, Chemical, and Petrological Characteristics of Chondritic Materials and Their Relationships to Small Solar System Bodies. in *Primitive Meteorites and Asteroids* (ed. Abreu, N.) 59–204 (Elsevier, 2018). doi:10.1016/B978-0-12-813325-5.00002-1.
2. Jones, R. H. Petrographic constraints on the diversity of chondrule reservoirs in the protoplanetary disk. *Meteoritics & Planetary Science* **47**, 1176–1190 (2012).
3. Rubin, A. E. Physical properties of chondrules in different chondrite groups: Implications for multiple melting events in dusty environments. *Geochimica et Cosmochimica Acta* **74**, 4807–4828 (2010).
4. Russell, S. S., Connolly Jr., H. C. & Krot, A. N. *Chondrules: Records of Protoplanetary Disk Processes*. (Cambridge University Press, Cambridge, United Kingdom, 2018).
5. Scott, E. R. D. & Krot, A. N. Chondrites and Their Components. in *Meteorites, Comets, and Planets, Treatise on Geochemistry* vol. 1 143–200 (Elsevier B V, Amsterdam, 2003).
6. Brearley, A. J. & Jones, R. H. Chondritic Meteorites. in *Planetary Materials* 398 (Mineralogical Society of America, Washington, D.C. USA, 1998).
7. Hutchison, R., Bridges, J. C. & Gilmour, J. D. Chondrules: Chemical, Petrographic and Chronologic Clues to Their Origin by Impact. in *Chondrites and the Protoplanetary Disk* vol. 341 933–950 (San Francisco, CA, 2005).
8. Hewins, R., Connolly, H. C., Lofgren, G. E. & Libourel, G. Experimental constraints on chondrule formation. in *Chondrites and the Protoplanetary Disk* vol. 341 286–316 (2005).
9. Hewins, R. Chondrules. *Annual review of Earth and Planetary Sciences* **25**, (2024).
10. Marrocchi, Y. *et al.* Chondrule properties and formation conditions. *Space Science Reviews* **220**, 69–168 (2024).
11. Lauretta, D., Nagahara, H. & Alexander, C. Petrology and Origin of Ferromagnesian Silicate Chondrules. in *Meteorites and the Early Solar System II* (The University of Arizona Press, Tucson, AZ, 2006).
12. Rubin, A. E. & Wasson, J. T. Chondrules in the Murray CM2 meteorite and compositional differences between CM-CO and ordinary chondrite chondrules. *Geochimica et Cosmochimica Acta* **50**, 307–315 (1986).
13. Olsen, M. B., Wielandt, D., Schiller, M., Van Kooten, E. M. M. E. & Bizzarro, M. Magnesium and 54Cr isotope compositions of carbonaceous chondrite chondrules – Insights into early disk processes. *Geochimica et Cosmochimica Acta* **191**, 118–138 (2016).
14. Libourel, G. & Portail, M. Chondrules as direct thermochemical sensors of solar protoplanetary disk gas. *Science Advances* **4**, 1–12 (2018).
15. Rubin, A. E., Dunn, T. L., Garner, K., Cecchi, M. & Hernandez, M. Barred olivine chondrules in ordinary chondrites: Constraints on chondrule formation. *Meteoritics & Planetary Science* **59**, 670–684 (2024).
16. Noguchi, T. Estimation of three-dimensional internal structures of some barred olivine chondrules in Allende (CV3) chondrite. *Antarctic Meteorite Research* **15**, 59–77 (2002).
17. Tsuchiyama, A., Osada, Y., Nakano, T. & Uesugi, K. Experimental reproduction of classic barred olivine chondrules: open-system behavior of chondrule formation 1. *Geochimica et Cosmochimica Acta* **68**, 653–672 (2004).
18. Lofgren, G. & Russell, W. J. Dynamic crystallization of chondrule melts of porphyritic and radial pyroxene composition. *Geochimica et Cosmochimica Acta* **50**, 1715–1726 (1986).

19. Connolly, H. C. & Hewins, R. H. Chondrules as products of dust collisions with totally molten droplets within a dust-rich nebular environment: An experimental investigation. *Geochemica et Cosmochimica Acta* **59**, 3231–3246 (1995).

Supplementary Files

This is a list of supplementary files associated with this preprint. Click to download.

- ThomasKeprtaSupplemental.zip
- SupplementaryDataVideo1OREX803079241Media.mp4
- SupplementaryDataVideo2OREX803079241individualfragment.mp4
- SupplementaryDataVideo3OREX803417103Media.mp4
- NGSemailattachmentSMC17713492331.pdf